Validation of non-destructive testing techniques for additive manufacturing

Joana Rafaela Ferreira Antunes

Thesis to obtain the Master of Science Degree in

Mechanical Engineering

Supervisors: Prof. Maria Luisa Coutinho Gomes de Almeida
Eng. Ana Beatriz Mendes Lopez

Examination Committee

Chairperson: Prof. Rui Manuel dos Santos Oliveira Baptista
Supervisor: Eng. Ana Beatriz Mendes Lopez
Members of the Committee: Prof. Telmo Jorge Gomes dos Santos
Prof. Carlos Manuel Alves da Silva

November 2019

Agradecimentos

Em primeiro lugar, gostaria de agradecer à Prof. Luisa Coutinho pela possiblidade de realizar este trabalho num tema e projeto de tamanha relevância para a indústria como a iremos conhecer futuramente. Obrigada não só pela orientação nas alturas de maior incerteza, como pela disponibilidade que sempre demonstrou ao longo deste trabalho.

À Ana Lopez, um obrigada não será suficiente para reconhecer o apoio incansável tanto a nível técnico como pessoal ao longo destes seis meses. No fim desta jornada, posso dizer que não poderia ter tido melhor orientação neste trabalho, ou maior inspiração para esta nova fase que se avizinha.

Não poderia deixar de agradecer ao professor Telmo, assim como toda a equipa do Laboratório de Ensaios-Não-Destrutivos no UNIDEMI da FCT UNL, a quem reconheço todo o apoio técnico e sentido critico prestado em grande parte deste trabalho.

Ao LABEND do ISQ, obrigada ao Eng. José Pedro e a toda a equipa não só pela recepção e contribuição a nível técnico, mas também pela visão mais empresarial da investigação que me permitiram experienciar.

Aos amigos que tive o privilégio de conhecer nesta aventura, obrigada pelas horas de estudo que se tornaram mais divertidas e pelo companheirismo que espero manter para a vida. Em especial, queria agradecer à Mónica, o denominador comum a estes 5 anos e certamente aos próximos, pela amizade e compreensão em todos os momentos.

Ao Francisco, obrigada por todo o apoio nos pontos altos e baixos deste trabalho, mas acima de tudo, obrigada por todo o carinho e dedicação nestes dois últimos anos.

Por fim, gostaria de dedicar este trabalho aos meus pais e irmão, por todos os sacrifícios que fizeram que me permitiram ter o acesso à educação que tive nestes últimos cinco anos, sem nunca olharem a custos e medidas para me darem sempre o melhor. Pelos valores que me instituiram e o apoio incondicional, aos meus pais, devo tudo.

Resumo

Este trabalho consolida a aplicação das técnicas de inspecção por correntes induzidas (CI) e ultrassons (US) na inspecção de defeitos em tempo real em peças de aço de grandes dimensões produzidas a partir de fabrico aditivo por arco elétrico com fio consumível (WAAM). A tecnologia WAAM tem sido reconhecida como uma das mais economicamente viáveis para a produção de peças em indústrias como aeroespacial, petróleo e gás, arquitectura, energias renováveis, entre outras. No entanto, de forma a que o fabrico por WAAM possa ser implementado com sucesso nesses sectores, sistemas de ensaios não-destrutivos (END) devem ser desenvolvidos de forma a garantir a qualidade das peças produzidas.

O aço-carbono carece de investigação no setor de END em WAAM, uma vez que o progresso feito neste tópico foi alcançado maioritariamente em alumínio. Este aço enfrenta vários desafios de inspecção devido às suas propriedades ferromagnéticas, textura superficial e altas temperaturas inerentes à deposição. Recorrendo às CI, foi desenvolvida uma sonda personalizada para atingir maiores profundidades de penetração e superar as limitações do material. Nos US, um modelo computacional, validado experimentalmente, foi desenvolvido para avaliar o efeito da ondulação na inspecção por US *phased array* (PAUT). Finalmente, o uso de pasta de soldadura como acoplante de US em alta temperatura foi também estudado.

Os resultados exibem o potencial de ambos os métodos serem utilizados de forma complementar na inspecção. Ambos permitiram detectar defeitos nas profundidades requeridas e a pasta de soldadura mostrou grande potencial para ser usada como acoplante num cenário de inspecção realista.

Palavras-chave: Fabrico aditivo por arco elétrico com fio consumível, ensaios não destrutivos, correntes induzidas, ultrassons.

Abstract

This work consolidates the application of both eddy current (EC) and ultrasonic (UT) techniques for the in-line inspection of defects on large Wire Arc Additive Manufacturing (WAAM) steel parts. WAAM technology is being recognized as one of the most cost-effective manufacturing processes for large part production in industries such as aerospace, oil and gas, architecture, renewable energies, among others. However, before WAAM can be successfully implemented in these sectors, non-destructive testing (NDT) systems must be developed in order to produce quality assured finished components.

Carbon-steel lacks investigation in the WAAM NDT field as progress on this topic was achieved mainly on aluminum. This material faces many inspection challenges due to its ferromagnetic proprieties, surface texture and high temperatures during deposition. Regarding EC, a new customized probe was developed to reach higher penetration depths than its predecessors and overcome the magnetic limitations. In the UT field, a realistic computational model for phased array UT (PAUT) was designed to evaluate the waviness effect on defect detectability, which was experimentally validated. Moreover, the effect of using solder paste as UT couplant for high temperature inspection was also studied.

Experimental outcomes show the potential of both inspection methods for being used complementary in both non-ferromagnetic and ferromagnetic materials depending on part geometry. Both EC and UT techniques were able to detect defects on the required depths and the solder paste showed great potential to be used as a couplant on a realistic inspection scenario.

Keywords: Wire and arc additive manufacturing, non-destructive-testing, eddy current testing, ultrasonic testing.

Contents

List of Tables

List of Figures

List of software

ANSYS© Maxwell 3D

Autodesk PowerMill©

Extende CIVA©

LabVIEW™

MATLAB©

SolidWorks©

List of Acronyms

AF - Acicular ferrite
AM - Additive manufacturing
AC - Alternating current
BJ - Binder jetting
CMT - Cold Metal Transfer
CT - Computed tomography
CNC - Computer numerical controlled
DOE - Design Of Experiment
DED - Direct energy deposition
DMLS - Direct metal laser sintering
ECT - Eddy current testing
EBM - Electron beam melting
EDS - Energy dispersive x-ray spectrometer
FEM - Finite elements method
GMAW - Gas Metal Arc Welding
GTAW - Gas Tungsten Arc Welding
GF - Grain boundary ferrite
LOM - Laminated Object Manufacturing
XBT - X-ray backscatter technology
NDT - Non-Destructive Testing
PAUT - Phased Array Ultrasonic Testing
PAW - Plasma Arc Welding
PWD - Plasma Wire Deposition
PLA - Polylactic Acid
PBF - Powder bed fusion
IQI - Quality indicator
SEM - Scanning electron microscopy
SLM - Selective laser melting
SL - Sheet lamination
SEP - Sideways Excitation Probe
SNR - Signal to noise ratio
TS - Travel speed
TIG - Tungsten Inert Gas
UT - Ultrasonic testing
WAAM - Wire arc additive manufacturing
WFS - Wire feed speed

Chapter 1

Introduction

1.1 Motivation

Additive manufacturing (AM) has become one of the most revolutionary technology applications in manufacturing. Once employed mainly for prototyping, AM today holds the potential to completely change the way products are designed and built. The peak of its impact will come from using this technology to produce both high strength and high integrity metals for applications in large engineering structures. By doing this effectively and on a large scale, AM promises to transform major engineering sectors such as energy, aerospace and construction.

Following this industry need the LASIMM project was created with the aim to develop a a Large Additive/Subtractive Integrated Modular Machine (LASIMM) with capabilities for AM, machining, cold-work, metrology and inspection. Figure 1.1 shows a steel part produced for Foster + Partners, one of LASIMM's partner companies, for structural applications.

Figure 1.1: Structural steel part (LASIMM - internal report).

One of the main research challenges of this project is to find suitable methods for ensuring the quality and structural integrity of the parts produced. Hence, the necessity of developing Non-Destructive Testing (NDT) systems emerges, as these are of extreme importance to detect defects as early as possible in the manufacturing process, avoiding material wastage. Additionally, doing this inspection layer by layer allows the possibility to remove the last flawed deposit with an adequate subtraction process.

According to Lopez et al. [1] both ultrasonic (UT) and eddy current (EC) techniques have been identified has having the potential to be used in the in-line inspection of AM metal parts fabricated using wire + arc additive manufacturing (WAAM), a direct energy deposition welding process. However, most of this previous research on NDT for WAAM was centred on aluminium. Carbon steel is one of the most accessible metals in the AM printing market, and can be used under different types of alloys making it even more attractive for industries with their own requirements. This material faces many inspection challenges due to its ferromagnetic proprieties, surface texture and high temperatures during deposition [2, 3]. That being said, the main focus of this dissertation was the consolidation of the mentioned NDT techniques for the case of steel, as the use of this material implies surpassing many technological challenges before adquate inspection.

1.2 Objectives

In order to contribute for the identification of the application field of UT and EC techniques for the in-line non-destructive inspection of steel parts fabricated by WAAM, the two following objectives must be accomplished:

- **Manufacturing process optimization for surface texture minimization:**

  WAAM steel reference samples have to be manufactured in order to assess the capabilities of the NDT techniques. To do so, minimum surface texture should be attained as it is a characteristic of the process that tends to hinder both UT and EC techniques [4, 5].

- **Consolidation of ECT and UT techniques for the detection of internal flaws in WAAM parts:**

  Each NDT method comes with it's own set of benefits and limitations. In EC testing of ferromagnetic materials like carbon steel, the magnetic permeability variations can conceal the orderly location of a defect. In UT, surface texture and adequate high-temperature coupling are the main challenges to overcome.

1.3 Thesis Outline

The structure of this thesis is divided into 6 chapters with its format being the following:

Chapter 1, the current one, consists in the introduction to the topic under discussion, focusing on the motivation and objectives of the further chapters.

In **chapter 2**, a more detailed presentation into AM is made along with a brief mapping of the its different available processes. Then, the focus shifts to WAAM itself, from process variables to common defects. A review of different NDT techniques is also presented and explained. This is done by summarizing the basic concepts of each method as well as presenting the results obtained in the field of WAAM.

For the following three chapters, it is important to note that this thesis followed a homogeneous structure where the results and their discussion are done simultaneously. Moreover, the methods are presented mostly in the beginning of each chapter, but sometimes throughout it when necessary. This was done to simplify the reading as methods and equipments are used for different reasons across the document.

Chapter 3 is based around the steel samples' manufacture, while optimizing process variables to accommodate surface texture for the benefit of inspection. This was done while keeping the structural integrity of the WAAM walls. The influence of the deposition strategy on the surface quality is one of the main focuses of the chapter.

Chapter 4 is dedicated to EC testing. In this section, a comparison is drawn between the past results on aluminium and the ones obtained in steel as this techniques is highly dependent of the material's magnetic proprieties. A new probe design is studied using the finite elements method (FEM) and its inspection capabilities were experimentally validated.

Chapter 5 regards UT inspection and is divided in two main parts. In the first section, a numerical analysis of the UT beam is done, along with some inspection simulations with the objective of understanding the impact of surface waviness in the acoustic behaviour. In the second section, the innovative use of solder paste as high temperature UT couplant is evaluated.

Lastly, **chapter 6** presents the overall conclusions from this work, as well as suggestions for future developments in the continuation of this thesis.

Chapter 2

Literature Review

2.1 Additive Manufacturing

Additive manufacturing (AM), as opposed to the subtractive approach, is an industry standard term defined as the process of joining materials layer upon layer. To do so, the material is deposited over a substrate, and subsequent layers are added in order to produce the final part.

Currently, AM is facilitating new opportunities in terms of today's production paradigm and manufacturing possibilities by enabling the fabrication of moderate to mass quantities of products that can be customized individually. With this technology, manufacturing lead times are reduced substantially and costumer demand can be met more quickly [6].

However, recent media enthusiasm caused by the expansion of AM technology for a wide range of materials has created the expectation that, in the near future, any material would be able to be printed into any size and shape. In theory, any object should be able to be sliced and rebuilt using those exact same layers, but although the technology is moving in that direction, this is not yet the case. In general, AM is still facing challenges regarding its production times, size restrictions, cost and regulations.

2.1.1 Socio-economic and environmental impact

AM has been considered one of the twelve potential disruptive technologies which will lead to the next industrial revolution by year 2025 [7]. The development of AM technologies has the potential to affect not only industry as a whole, but also business and society. According to Verhoef et al. [8], AM is growing by 33% a year and is starting to cover all sectors of industry as the market size is expected to reach more than USD 20 billion by 2020.

The impact of AM technologies becomes clear when reviewing its applications on different industries. For example, the aerospace business is one of the main sectors interested in the development of this technology mostly due to AM's biggest promise: reducing part costs by reducing time to market and material wastage. By removing constraints related to traditional manufacturing processes regarding both physical and financial feasibility limitations, AM has the potential for numerous design-related advancements in aircraft. These design improvements are, or will be, manifested primarily in terms of weight reduction and increased performance characteristics [9].

In medicine, AM is opening the door to a new approach in the production of medical devices by allowing the complexity of their designs to be pushed to the extreme. Culmone et al. [10] explains that this can be a great opportunity to provide easy access to healthcare in developing countries as well as an important step toward patient-specific medicine.

From an environmental standpoint, AM holds the potential to reduce the carbon footprint through design optimization and reducing material wastage. According to Frazier [11], the ATKINS project concluded that an optimal AM design could show a weight and material saving of almost 40%. The analysis showed that for a long range aircraft, reducing the weight by 100 kg results in a 2.5 million dollar saving in fuel over the lifetime of the aircraft.

AM has taken the industry by storm, enabling manufacturers to bring products to market faster, for less. Today, developments made on metal AM and numerous applications of the process are moving to the forefront of manufacturing, which will be discussed on the next section.

2.2 Metal Additive manufacturing

According to Martina [12], heat source, raw material and a manipulator, are the three main constituents essential for metal AM. The first is necessary for raising the temperature above the raw material's melting point. The second, raw material, can be fed in various forms, with wire and powder being the most popular. Finally, the manipulator traces the tool path defined for each layer.

Regarding the heat source, most come from the welding world, with torches, laser and electron beams being the most relevant examples. The combination of different heat sources and materials leads to different metal AM techniques, each characterized by its features, advantages and limitations. Figure 2.1 presents a mapping of different technologies for metal AM. As can be seen, this processes can be sorted by Binder jetting (BJ), Sheet lamination (SL), Powder bed fusion (PBF) and Direct energy deposition (DED). The following review of each will be directed with one of the main LASIMM objectives in mind: to create large scale metal structures.

- BJ is a process carried out at low temperatures that involves depositing a liquid binder on a powder layer, as illustrated on figure 2.2 a). When the binder dries, mechanical strength is given to the mix by curing. Then, the part is heat treated to sinter or consolidate the loose powder achieving a uniform composition of a single alloy [14]. The BJ technology holds the capability of handling metals/alloys and ceramics (including glass, sand and graphite). One of its most relevant benefits is that there are no residual stresses created in the parts, as this method does not involve heating during the building process. However, it involves several post-processes that follow the printing of the parts such as curing, de-powdering, sintering, infiltration, annealing, and finishing. These post-processes sometimes take longer time than the actual printing itself and may incur in significant costs [15]. Moreover, the parts are expected to have a coarse microstructure, due to the thermal treatments. Hence, the mechanical properties of the parts become compromised. For these

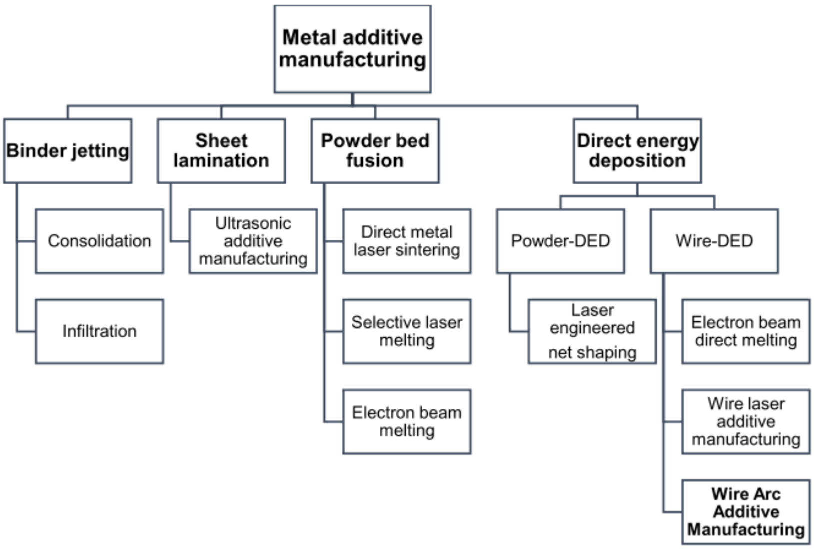

Figure 2.1: Metal additive manufacturing technologies [13].

reasons, the material characteristics are not always suitable for structural applications in aerospace and automotive parts.

- SL uses precision metal sheets that are usually cut with CNC to create the desired geometry of the part [14]. One of the first commercialized additive manufacturing techniques was Laminated Object Manufacturing (LOM), represented on figure 2.2. The process done a low temperatures and allows for internal geometries to be created. This requires relatively little energy, as the metal is not melted. Benefits include low cost and cutting can be very fast due to the cutting route only being that of the shape outline, not the entire cross sectional area. However, the main disadvantage is related to the weakness of the material, because the strength and integrity of the models is reliant on the adhesive used.

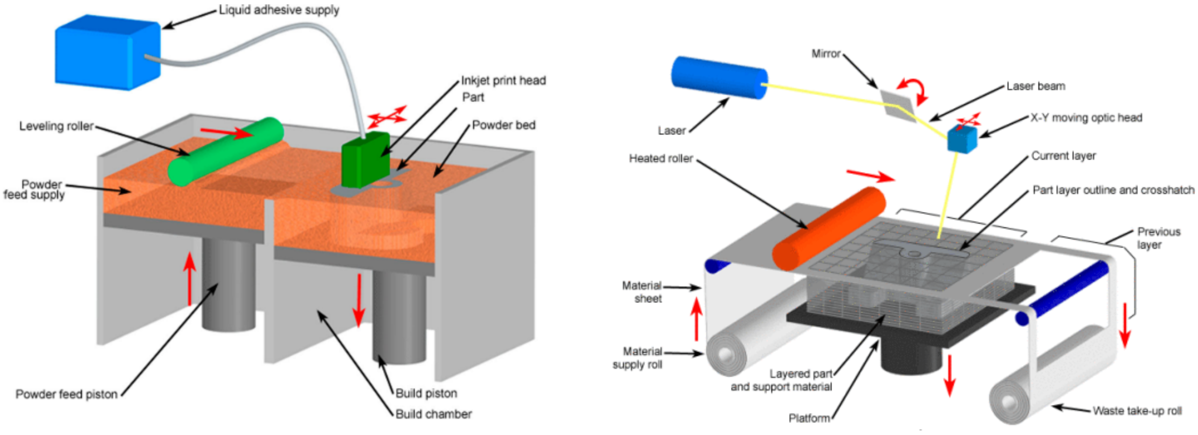

(a) BJ [14].

(b) LOM [16].

Figure 2.2: BJ and SL techniques schematics.

- PBF is a process where 3D parts are produced by selectively melting portions of a powder bed layer-by-layer according to input CAD geometry using a scanning energy source [17]. The primary difference between its variants comes from the source of energy (laser or electron beam) and if the metal in melted of sintered: Selective laser melting (SLM, figure 2.3 a)), electron beam melting (EBM) and direct metal laser sintering (DMLS). These three methods represent the vast majority of industrial and academic applications and research initiatives regarding metal AM. A wide range of engineering materials are processable using PBF including stainless steel, aluminum alloys, Ti-6Al-4V, and nickel superalloys. The parts produced frequently exhibit excellent static mechanical properties equivalent or superior to their traditionally manufactured counterparts. However, PBF processes are also known to induce a wide range of material defects such as gas porosity, key-hole porosity, and large lack-of-fusion defects. Also excessive and anisotropic residual stresses (RS) are frequently developed [18]. Although high complexity components can be achieved, PBF techniques aren't adequate to large part production as build rates are significantly lower when compared to its competitors.

- DED technologies are those where focused energy by an electron beam (seen in figure 2.3 b)), laser or arc, generates a molten pool into which feedstock in the form of powder or wire is deposited on the substrate surface [14]. Wire-DED uses a feedstock of material in form of wire with an energy source such as electron beam, laser beam or arc. Wire feed systems are adequate for large part production due to having high deposition rate processing and large build volumes making them adequate. However, more extensive machining is usually required when compared to powder bed or powder fed systems due to the irregular surface finishing. Wire Arc Additive Manufacturing, a combination of an electric arc as heat source and wire as feedstock, is the core of this work and will be explained in more detail on the next section.

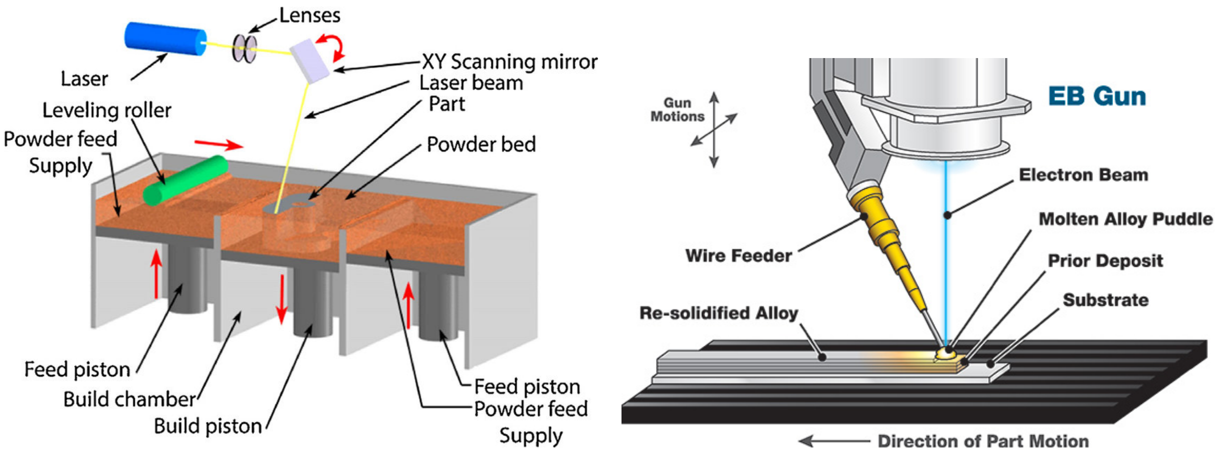

(a) Selective laser melting (SLM) [19].

(b) Electron beam, wire-fed DED system [14].

Figure 2.3: Powder bed fusion (PBF) and direct energy deposition (DED) techniques.

2.3 WAAM

Compared to other AM techniques for metals, "WAAM is one of the most promising techniques for fabricating large components with moderate complexity and relatively low costs", according to [20]. It is performing exceptionally well in the production of lightweight aerospace components (landing gear parts, wing ribs or stiffeners), wind tunnel models and complex constructive features that could not be made with conventional processes such as casting, or computer numerical controlled (CNC) milling [20]. Williams et al. [21] explains that WAAM uses standard welding equipment as hardware: welding power source, torches and wire feeding systems. Motion is provided either by a robotic system or an addapted CNC machine.

The main objective of this chapter is to summarize the influence of process conditions on the mechanical and surface properties of parts. But first, it is necessary to understand the different types of WAAM variants that exist. Those come from: Gas Metal Arc Welding (GMAW), Gas Tungsten Arc Welding (GTAW) and Plasma Arc Welding (PAW), all represented on figure 2.4

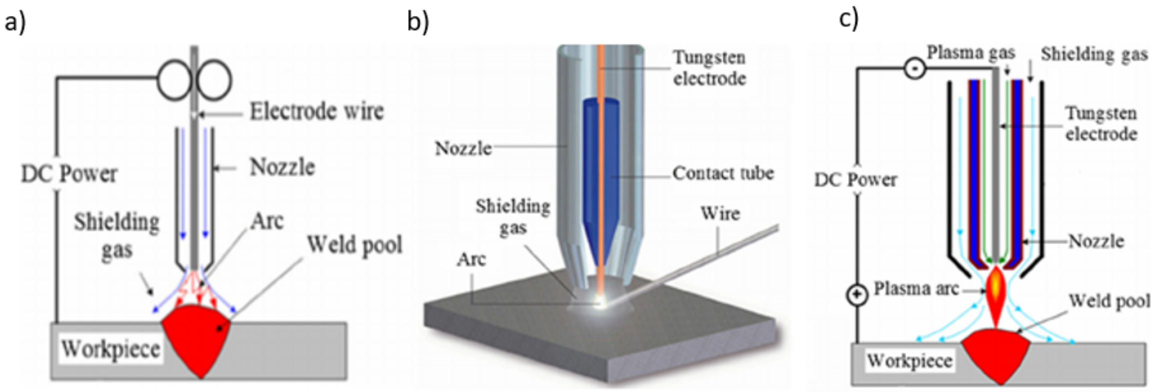

Figure 2.4: GMAW, GTAW and PAW welding variants, respectively [22].

In GTAW and PAW an electric arc forms between a non-consumable tungsten electrode and the workpiece. Both processes use an inert shielding gas envelope (Argon and/or Helium) to protect the weld pool. In both variants, the wire is not supplied within the torch. For that reason, in order to ensure deposition consistency, the wire must be fed from the same direction no matter the orientation of the deposited layer. This requires rotation of the torch and consequently leads to complicated robot programming [23, 24].

GMAW is the most common industrial welding process mainly due to its versatility, but it is also the first choice for WAAM purposes when possible. The consumable wire electrode is fed coaxially with the welding torch and perpendicularly to the substrate resulting in an easier tool path which improves the material deposition efficiency and leads to a simpler adaptation of the process to robot automation. This process is also frequently chosen due to its high deposition rates which are imperative to reduce the lead time of large metal parts when compared to subtractive methods [21]. In GMAW, an electric arc forms between a consumable wire electrode and the metal substrate. A shielding gas is used in both subtypes to protect the welding pool from the atmospheric environment and improve the stability of the electric arc.

Finally, in addition to these processes there is also Cold Metal Transfer (CMT), which is a ”modified GMAW variant that relies on controlled dip transfer mode mechanism to provide beads with good quality, lower thermal heat input and nearly without spatter”, according to Williams et al. [21]. This was the variant used within the experimental work of this thesis, and will be furthered explained in the next subsection.

2.3.1 Cold metal transfer

CMT was firstly introduced by Fronius [25] in 2004 promising higher deposition rates for the metal additive manufacturing community and it is a considered a “cold” process when compared to other arc welding methods. Due to the fact that conventional arc welding usually has an unstable arc and a lot a splattering, many researchers have gained interest towards CMT when Fronius claimed that it was the most stable weld process in the world. Sequeira Almeida and Williams [26] claimed excellent quality weld beads, extremely stable arc, lower heat input than the other DED-methods, and nearly spatter free process when using CMT. It is also easy to operate, handle and combine with robotic systems.

CMT controlled dip transfer mechanism consists in dipping the molten droplet into the weld pool and then drawing it back forcing the droplet to detach by the action of the wire forces, as illustrated on figure 2.6. This backwards movement reduces the spatter significantly, since no droplets transfer from the gap between the wire and base material.

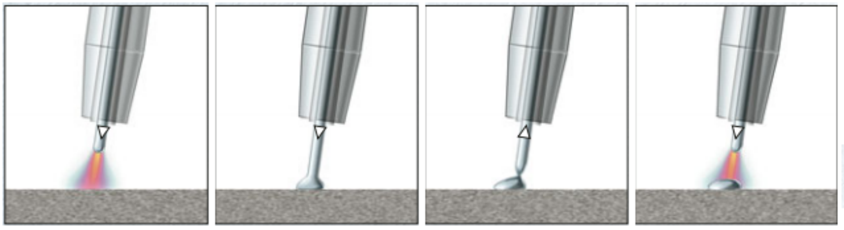

Figure 2.5: CMT process steps [27].

There are three main phases on a CMT cycle: short-circuit phase, boost phase and burn phase, as seen on figure 2.6. Boost and burn phase together forms the arcing phase, referring the time that the arc is on. This on/off-arcing leads to lower heat input than the traditional arc welding methods [27].

Mezrag et al. [28] defined a CMT cycle by having the following steps:

1. The **boost phase** starts when the arc is ignited. Wire feed can be considered in a static position and the wire top is starting to form a liquid drop.
2. When the **burn phase** starts, current decreases to avoid the detachment and growth of the droplet and the wire feed rate increases until it the short-circuit phase begins (when the droplet touches the weld pool).

The voltage of the arc is constant in the boost phase, but decreases in the wait phase, since arc length is decreased. The wait phase duration is determined by the time that is required for the wire tip to touch the substrate material . In the short-circuit phase the voltage is near zero and the wire feed rate is backwards. The backward movement forces the melted material to form a narrow bridge between the droplet and the wire and, with the aid of surface tension, the molten droplet is detached from the wire

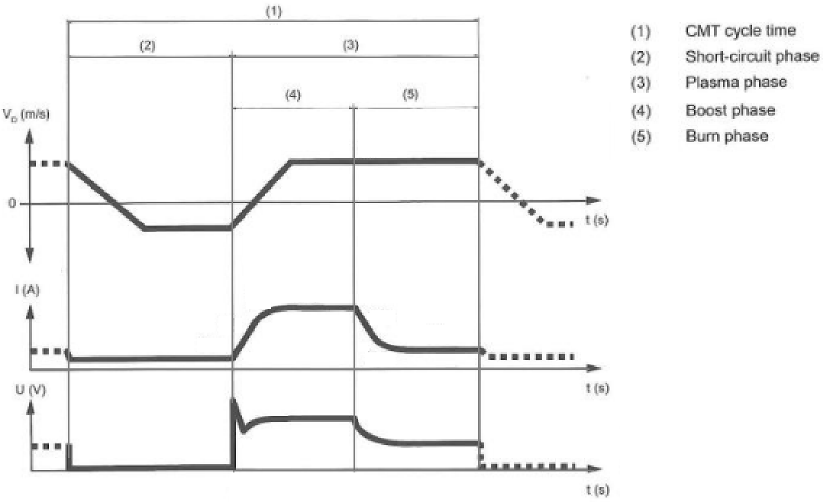

Figure 2.6: CMT characteristics showing the variations of wire feed rate, current and voltage. Adapted from [27].

and the arc is reignited. The duration of the short-circuit phase is dependent on the time that is required to detach the molten droplet [28].

To start the welding process, the user chooses the material, wire diameter, gas, wire feed speed and Fronius black box defines the rest. This black box is usually referred as the synergic line. This lines were created by Fronius via special measurement technology for each material and wire diameter. Välimäki [27] suggests that synergic lines act similarly between materials but the magnitudes differ due to the material properties. The synergic lines play a significant role on keeping the wire feed rate and current in balance with the voltage in order to maintain arc stability. This is dependent on the thermal and electrical resistivity of the wire. Typically the wire feed rate is limited by the energy of the heat source. When there is high wire feed rate, the energy used has to be high as well in order to fully melt the particles [28].

2.3.2 Process parameters influence on bead geometry

It is particularly important to develop mathematical models to predict the effect of the process parameters upon geometry. By doing so, the most appropriate parameter combinations can be chose to minimise waste, maximise productivity and enable automation. Martina [12] explains that ultimately, ”this set of process equations is required for the development of Computer-Aided Manufacturing (CAM) software”.

With this objective in mind, Martina et al. [23] developed some empirical relationships between process parameters and walls geometry for Plasma Wire Deposition (PWD) WAAM by adopting a Design Of Experiment (DOE) approach. Martina [12] used the same method for developing a TIG based WAAM process model.

In the case of CMT, the process used on this thesis, bead geometry is highly affected by wire feed speed (WFS) and travel speed (TS). The increase of WFS results in more material input to the system and, depending on the TS, it determines how much material is input per unit of length. Hence, Sequeira Almeida and Williams [26] started a systematic process analysis which led to the development of a reliable geometric model for CMT. The authors selected WFS and WFS/TS ratio in order to ensure constant material deposition per unit length. Consequently, it became possible to predict a series of responses from the input data, as can be observed on figure 2.7. This process analysis will be the one used further on the experimental procedure of chapter 3.

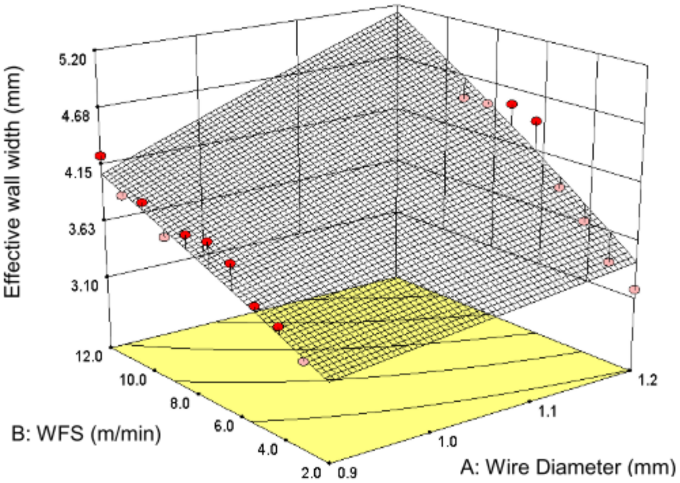

Figure 2.7: Surface model for the effective wall width response as a function of the wire diameter and the WFS, for constant WFS/TS ratio of 20 [26].

2.3.3 Microstructure and mechanical proprieties

During fabrication, AM metal parts experience a complex thermal history involving directional heat extraction, and repeated melting and rapid solidification. According to Frazier [11], ”many alloys also experience repeated solid state phase transformations”, which introduce complexities that are especially important to the control and optimization of the material's properties. Moreover, the feedstock composition also affects the produced metallurgy of the material.

Even though there are different AM processes, the melting metallurgical principles are very similar between them. The solidification kinetics are determined by the weld pool geometry which is affected by travel speed, power and size of the heat source. Phase formation, grain growth and kinetics of the precipitations are determined by the thermal history, such as thermal cycling and cooling [14, 29]. According to Sames et al. [14], the microstructures vary between processes as the thermal gradient is one of the key factors in microstructure evolution, especially when comparing AM to casted parts [29].

One of the major concerns in AM is anisotropy. The unidirectional heat flow into a substrate forms textured grains and anisotropic properties. Texture in material science means that polycrystalline material grains have preferential crystallographic orientation. When that happens, the part will have directional properties, which is called anisotropy. Typically, AM produced parts have an oriented grain structure, which can mean that the mechanical properties differ in direction. For this reason, it is important to always present the orientation of the build in the mechanical test results.

2.3.4 Common defects

According to Rodrigues et al. [2], ”predominant macro defects appear once layers start to be built in WAAM”. These include: side collapse, stuck unmelted wire and large distortions upon unclamping. Moreoever, certain materials tend to be vulnerable to specific defects, as shown in figure 2.8. In the case of steel, cracks, deformation and surface finish seem to be the most worrisome aspects to look out for. The main reason for the emergence of these types of defects in WAAM seems to be improper selection and control of processing parameters, as well as excessive heat input, gas contamination, and feedstock quality [3].

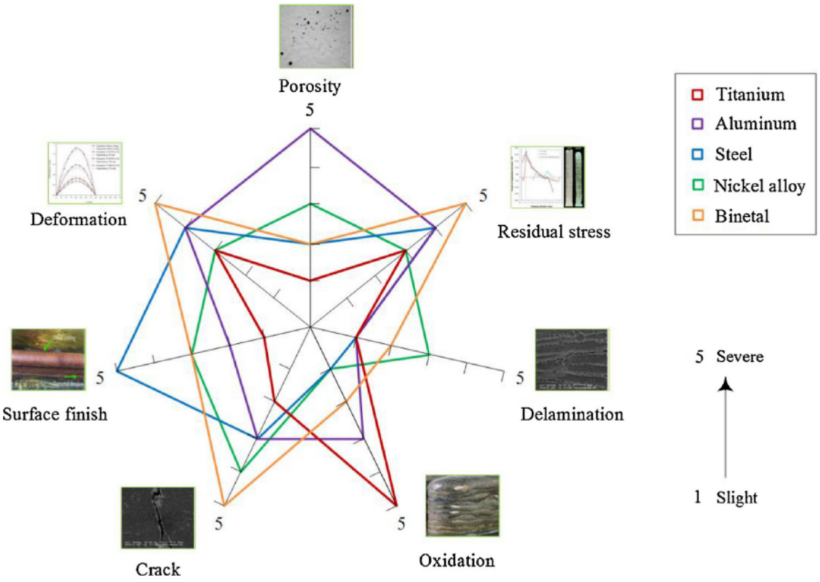

Figure 2.8: The correlation between materials and defects in WAAM processes [3].

Due to the fact that WAAM is an adaptation of a welding process, it is inferable that the defects found in WAAM parts will be similar to the ones found in welding beads, such as cracking, porosity, lack of fusion, inclusions, humping, etc. Both the International Standard ISO 65201 and 6520-1 can be used in order to establish some criteria for the defects, due to the mentioned similarities.

Generally, WAAM parts require post-process treatment to improve material properties, reduce surface roughness and porosity, and remove residual stress and distortions. Presently, several technologies have been reported to improve part quality in the WAAM process such as post-process heat treatment, interpass cold rolling, peening and ultrasonic impact treatment and interpass cooling [30, 31].

Nowadays, with all the advancements made on WAAM process control, it can be said that the challenge isn’t to produce parts with little to no defects, but the in-line detection and identification of those when they do exist. This goal can be reached by allowing in-process non-destructive testing and repair by layer machining, which is one of the goals of the LASIMM project. With this view of qualifying WAAM for industry applications, the knowledge on non-destructive testing techniques should be expanded, which will be the topic of the following chapters in this literature review.

2.4 Non-destructive testing

In order to successfully implement WAAM manufacturing of large scale engineering structures, it is of extreme importance to further develop on methods that are able to ensure the parts' structural integrity. Moreover, the lack of quality assurance standards can be said to be one of the main challenges that is hindering the acceptance of WAAM in the manufacturing industry. It is following this need that NDT systems come forth.

NDT allows detecting and evaluating flaws in materials or even differences in its characteristics, without compromising the serviceability. However, according to [4], high surface roughness or deep defects location can be seen as the main factors that challenge the application of NDT in AM. Not only that but the implementation of NDT during the process (in-line inspection), as opposed to post-operation, is pivotal. Presently, ”WAAM in-line inspection conditions are extremely demanding for current state of the art NDT probes”, as Rodrigues et al. [2] explains. The main problems include: high temperature of the last deposited layer; difficulty to obtain a high signal-to-noise ratio; surface waviness and roughness; and small defects dimension ($<$1 mm).

Lopez et al. [32] mapped the currently available NDT techniques suitable for WAAM. Imaging techniques such as X-ray backscatter technology (XBT) and computed tomography (CT) showed potential regarding de detection of deep and embedded defects, with CT already being able to uncover porosity ranging of 10–60 µm and defects in PBF AM parts [33, 34]. The problem with these imaging scanning techniques lies on the unacceptably long inspection times and size limitations. With radiographic testing, there are some safety limitations and difficulties in detection that are associated with the angle between the crack and the radiation. For those reasons, imaging techniques are not yet suitable for the in-line inspection of large WAAM parts.

Lopez et al. [1] concludes that, for in-process inspection EC, UT and thermography are the most suitable candidates. Regarding thermography, its one of the most well known NDT techniques for AM due to the fact that it has the advantage of being able to monitor the process during manufacturing from a certain distance. Furthermore, Montinaro et al. [35] used remote laser thermographic methodology as a mean to detect micrometric defects in metal additive manufactured samples. However, the author reported difficulty in obtaining accurate defect extension evaluations. Hence, with this in consideration, the two techniques chosen to be implemented in this work were EC and UT and therefore, each is further detailed in the following two subchapters.

2.4.1 Eddy Current testing

Eddy current testing (ECT) is a NDT method rested on the principle of electromagnetic induction discovered by Michael Faraday in 1831. The principle is the following: ”when an alternating current (AC) energizes a coil, it creates a time-varying magnetic field on the surroundings of the coil, which, in turn, induces a varying electromotive force around a conductor and, consequently, an electric current will flow through a closed path in this conductor” [5]. The EC flow in the material then creates a secondary magnetic field that affects the one previously generated by the coil, as seen on figure 2.9. EC circulate parallel to the surface of the test sample and perpendicularly to the HP and HS magnetic fields.

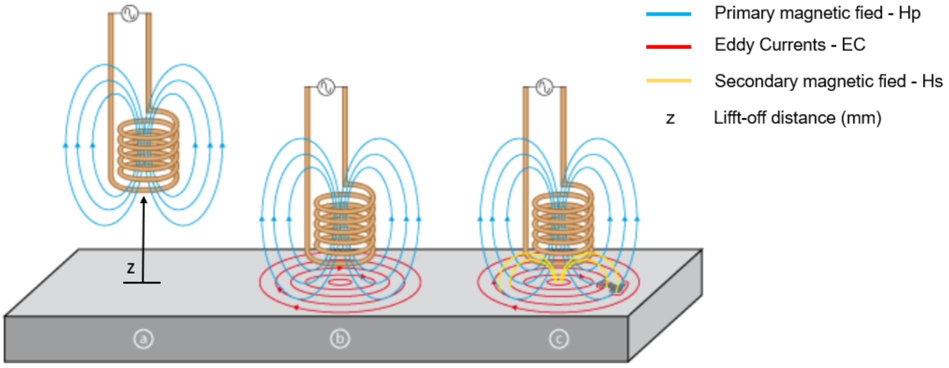

Figure 2.9: Principle of the NDT method using EC. Adapted [36]

Changes in metal thickness or defects like near-surface cracking, shown in figure 2.10, will interrupt or alter the amplitude and pattern of the eddy current and the resulting magnetic field. This in turn affects the movement of electrons in the coil by varying the electrical impedance of the coil. The eddy current instrument plots changes in the impedance amplitude and phase angle, which can be used by a trained operator to identify changes in the test piece.

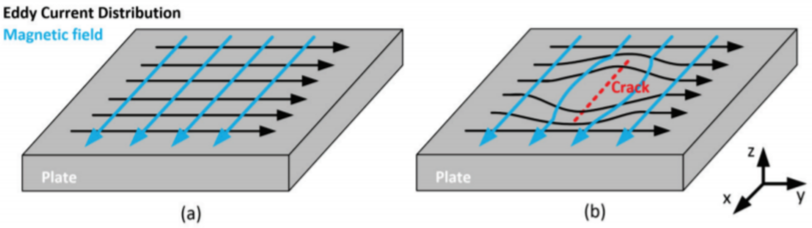

Figure 2.10: Representation of the eddy current flow with and without defects [37].

One of the constrictions of this method is that the inspected material has to be conductive for the EC to be generated and circulate within it. Higher the electrical conductivity of the material, lower the depth of penetration of the EC. The resistance to the flow of electricity is quantified by the magnitude of the electrical conductivity σ [S/m] or [%IACS] (International Annealed Copper Standard) where $\sigma_{\%IACS}$ = $1,7241 \cdot 10^{-6}\sigma_{S/m}$, or by its inverse, the electrical resistivity ρ $[\Omega.m]$ where 1 $\Omega.m$ = 1 m/S.

ECT presents a wide set of advantages compared to other NDT methods for the inspection of waam parts, such as not needing consumables or couplants, the possibility to implement without any direct physical contact between the probe and the inspected piece and permitting high-speed testing with practically instantaneous results [5, 32]. Although this advantages show the great potential of the application of ECT, the method presents some characteristics that can influence the behaviour of the EC and consequently limit it's use in WAAM in-line inspection. Those being the following.

Skin effect

The penetration depth of the EC is directly related to the skin effect. This phenomenon can be characterized by the fact that the EC concentrate near the surface adjacent to an excitation coil and their strength decreases with distance from the coil. Eddy current density decreases exponentially with depth, and this occurrence is known as the skin effect. The current density $J_z[A/m^2]$ depends on the depth z [m], and varies according to the equation 2.1:

$$J_z = J_0 \cdot e^{-z\sqrt{\pi \cdot f \cdot \mu \cdot \sigma}} \tag{2.1}$$

Where J_0 $[A/m^2]$ is the current density at the surface, f [Hz] is the excitation frequency used, μ [H/m] is the magnetic permeability of the tested material ($\mu = \mu_0 \cdot \mu_r$, which is the magnetic permeability of the vacuum μ_0 times the relative permeability μ_r of the material compared to the vacuum), and σ [S/m] the electrical conductivity.

From the last equation is possible to reach the standard depth of penetration δ [m] which corresponds the depth where the current density J_z is reduced to 37% ($e^{-1} \approx$ 0,37) of the superficial current density J_0:

$$\frac{J_z}{J_0} = e^{-1} \Leftrightarrow -z\sqrt{\pi \cdot f \cdot \mu \cdot \sigma} = -1 \tag{2.2}$$

Thereby, the standard depth of penetration δ [m] is presented as:

$$\delta_{(f,\mu,\sigma)} = \frac{1}{\sqrt{\pi \cdot f \cdot \mu \cdot \sigma}} \tag{2.3}$$

This does not guarantee that a defect located at that depth will be clearly detected, as it is only considered as a reference to find the optimal excitation frequency to reach a desired depth of inspection, knowing the characteristics of the material. This calculation is only reliable for the simplified case where the magnetic field penetrates in the material as plane waves (every ray parallel to one another), and considering a null lift-off (probe in contact with the inspected material).

Magnetic permeability

Magnetic permeability μ is a number that quantifies the degree of magnetic induction B of materials when a magnetic field H is applied, as shown in equation 2.4:

$$B = \mu \cdot H \tag{2.4}$$

Where $\mu = \mu_0 \cdot \mu_r$, with $\mu_0 = 4\pi \cdot 10^{-7}$ [H/m] and μ_r the relative permeability of the material compared to the vacuum.

Materials can be classified by their magnetic properties which strongly affect eddy current testing: ferromagnetic materials, like steel ($\mu_r \gg$ 1) and as non-ferromagnetic, for example aluminium, when $\mu_r \approx$ 1. High magnetic permeability makes the standard penetration depth decrease. Hence, in order to compensate for this effect and explore the material internally, ferromagnetic materials are inspected at lower frequencies.

The μ of a material is usually not constant resulting in a non-linear relationship between H and B.

Large variability in magnetic permeability is a characteristic of ferromagnetic materials. This permeability variation strongly influences the eddy current flow. The solution allowing the accuracy of the measurement of ferromagnetic materials is a process that equalizes permeability, such as a magnetization by means of a saturating direct-current coil. Saturated materials have a constant magnetic permeability and can be inspected with greatly reduced influence on permeability variations.

Edge effect

When a detection probe is placed near the edge of a specimen, eddy current flow is perturbed by the edge, which generates mixed signals with that of the defects. For this reason, the defect signal is difficult to distinguish when the EC probe is moved from the central area to the edge area.

With that in consideration, it is important that the diameter of the EC coil used in the testing is relatively smaller compared to the width of the deposited layer to avoid this problem when using conventional pancake-type probes. The limit to where each probe can approach the edges without suffering from this effect also varies with the type of EC probe used and needs to be tested accordingly.

Lift-off

The lift-off, distance between the probe and the test sample, is commonly known to be one of the main obstacles for effective eddy-current testing that leads to the erroneous results. A variation in the lift-off corresponds to an impedance change. This variation can be considered planar if the probe is detached away parallel to the surface and angular if the probe is moved obliquely in relation to the surface of the material.

Regarding the inspection of WAAM parts, the lift-off effect caused by the surface roughness is one of the main challenges to overcome when using ECT, according to Bento et al. [5]. This effect is undesirable and can be considered a background noise, since it can conceal the defect response by causing an impedance response with the same direction and/or bigger amplitude than the flaw.

2.4.2 Eddy current probes

Detecting flaws with different shapes and sizes can be very challenging using conventional pencil type probes, which are the most commonly used and commercially available. These probes operate in absolute bridge configuration which means the coils are located close to the test piece and are in an electric "bridge". The coils have double-functions: simultaneously generate and sense changes from the EC flow on the inspected sample. Any impedance variation of the coils is displayed as an absolute output signal on the complex impedance plane. These probes have the same advantages of simpler absolute probes, due to having the same kind of output signal, but their sensibility is higher due to the several coils close to the test piece [13]. This sensitivity to undesired variations can be problematic, especially when considering high surface texture, like the one found in WAAM parts.

With the objective of increasing the capability to detect flaws using EC: The IOnic probe was invented [38]. This probe induces EC on several directions into the material; increases the proximity of the probe with the test piece; and reduces the noise source from the planar lift-off and edge effects. As seen on figure 2.11, the IOnic Probe is composed by a toroidal excitation coil that generates EC into the material and is perpendicular to its surface and a planar spiral sensitive coil, which is subdivided in two semicircles wound in opposite directions that are perpendicular to the excitation coil and parallel to the inspected surface, to detect the perturbations of the EC flow in the material.

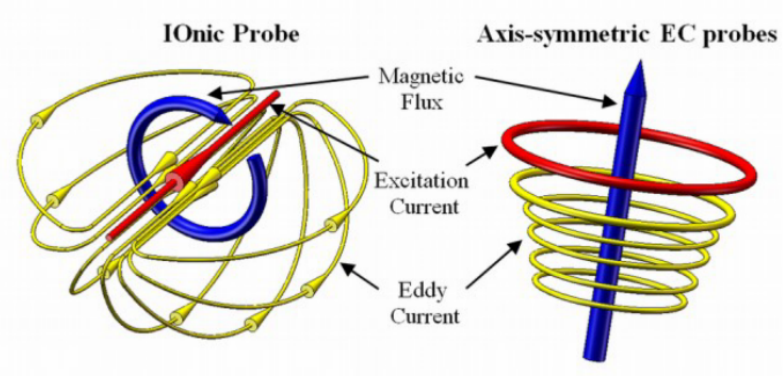

Figure 2.11: Eddy currents display in IOnic Probe (left) and conventional axis-symmetric EC probes (right) [39].

The *Modus operandi* of this type of probe revolves on the opposite winding of the sensitive coils which causes the magnetic field to have reversed intensities and therefore, to have two opposed contributions to the total current induced in the sensitive coil. When the impedance variations are compared between the two halves of the sensitive coil (differential mode), this results in a null value of the total current. According to [5], ”the difference in the potential is modified if the EC on one of the halves of the sensitive coil gets perturbed, for example by the detection of a defect”.

Bento et al. [5] developed customized probes for the in-line layer-by-layer detection of defects in aluminium WAAM samples. These are EC IOnic probes adapted to the weld bead curvature. This design proved to overcome the limitations caused by the surface roughness of the samples and the high temperatures involved in the deposition process. The latest version of this probe, the IOnic #3, was able to detect a slot with 350 μm of thickness, 2 mm bellow the surface, in a alluminum WAAM sample . This results showed that ECT is a promising solution for the in-line inspection of WAAM parts, since it detected defects at the required depths, while accommodating the curvature, roughness and high temperatures of the process. Because of the innovative design and potential of these customized IOnic probes, one of the objectives of this work is to test if they surpass the challenges of EC inspection in ferromagnetic materials, as will be studied in chapter 4.

2.4.3 Ultrasonic testing

Ultrasonic NDT is a technique used for characterizing the thickness or internal structure of a test piece through the use of high frequency sound waves. The frequencies used for ultrasonic testing are many times higher than the limit of human hearing, most commonly in a range from 500 KHz to 20 MHz. High frequency sound waves will travel through a medium until they encounter a boundary, at which point they reflect back to their source. By analyzing these reflections it is possible to measure the thickness of a test piece, or find evidence of cracks or other hidden internal flaws [40].

A typical UT inspection system consists of several functional units, such as the pulser/receiver, transducer, and display devices. A pulser/receiver is an electronic device that can produce high voltage electrical pulses. Driven by the pulser, the transducer generates high frequency ultrasonic energy. The sound energy is introduced and propagates through the materials in the form of waves. When there is a discontinuity (such as a crack) in the wave path, part of the energy is reflected back from the flaw to the surface. The reflected wave signal is transformed into an electrical signal by the transducer, as can be seen in figure 2.12, where the reflected signal amplitude versus the time from signal generation is displayed. Signal travel time can be directly related to the distance that the signal traveled. With this in consideration, information about the reflector location, size, orientation and other features can be obtained.

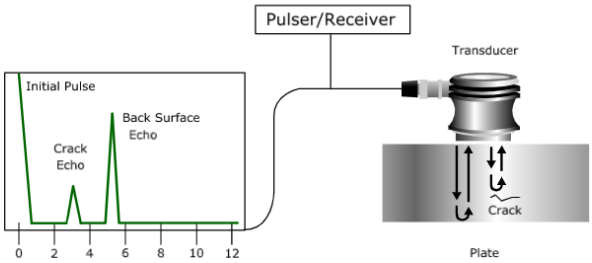

Figure 2.12: UT inspection system schematic [41].

Schmerr [42] explains that ultrasonic waves are mechanical waves originated by the vibration of the atoms or molecules that constitute a material, around their equilibrium positions, which means that this kind of waves cannot propagate in vacuum. There are several kinds of wave propagation types, each one with its own characteristics and speed, with longitudinal and transverse waves being the most commonly known. However, at surfaces and interfaces, various types of elliptical or complex vibrations of the particles form other types, such as Rayleigh and creeping waves. In longitudinal waves the oscillations occur in the direction of wave propagation. In transversal waves, the particles oscillate perpendicular to the direction of propagation and the vibrations excite the particles sinusoidally up and down due to a periodical shear force. These are relatively weak when compared to longitudinal waves.

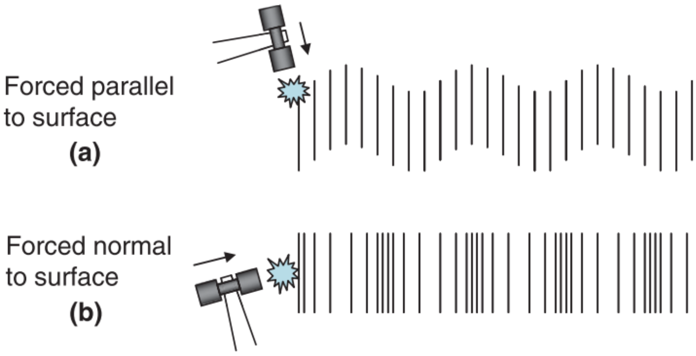

Figure 2.13: Longitudinal and traversal wave propagation [43].

The velocity of a wave is a vital parameter to UT in order to get correct and precise results. The velocity at which a sound wave propagates through a medium depends not only on the structure and geometrical shape but also on the medium itself. Its value can be obtained from wave equations that result from the elastic properties and density of the medium. Usually the longitudinal velocity of a wave propagating through a medium is twice the velocity of a tranversal wave, as Ihara [43] indicates. Sound wave velocity through a medium also changes with temperature, more specifically it reduces as the temperature increases and this values can vary by up to 1% per 55°C in steels [44]. The relationship between sound velocity and temperature is of extreme importance, especially in WAAM where temperature cycles in HSLA steel for example, range between 550 to 1150 °C [45], which can give rise to misleading results during inspection.

Incidence on an interface

Ultrasonic waves are reflected at boundaries where there is a difference in acoustic impedances (Z) of the materials on each side. This difference in Z is commonly referred to as the impedance mismatch. The greater the impedance mismatch, the greater the percentage of energy that will be reflected at the interface or boundary between one medium and another [46]. When the acoustic impedances of the materials on both sides of the boundary are known, the fraction of the incident wave intensity that is reflected can be calculated using equation 2.5 . The value obtained is known as the reflection coefficient.

$$R = \left(\frac{z_2 - z_1}{z_2 + z_1}\right)^2 \tag{2.5}$$

Where z_1 is the acoustic impedance of medium 1 and z_2 the acoustic impedance of medium 2.

When an ultrasonic wave passes through an interface between two materials at an oblique angle, and the materials have different indices of refraction, both reflected and refracted waves are produced. Refraction takes place at an interface due to the different velocities of the acoustic waves within the two materials, as can be seen in figure 2.14.

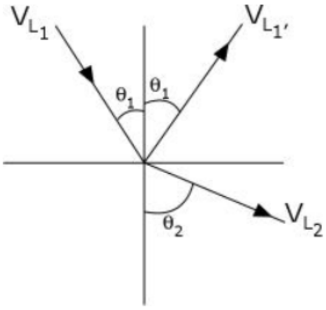

Figure 2.14: UT inspection system schematic [41].

The velocity of sound in each material is determined by the material properties such as elastic modulus and density. Snell's Law describes the relationship between the angles and the velocities of the waves by equating the ratio of material velocities V1 and V2 to the ratio of the sine's of incident and refracted angles, as shown by the following equation:

$$\frac{\sin\theta_1}{V_{L_1}} = \frac{\sin\theta_2}{V_{L_2}} \tag{2.6}$$

Where each θ is the angle measured from the normal of the boundary and V_L is the velocity of light in the respective medium.

Attenuation

When an ultrasonic wave propagates through a medium, attenuation is caused by a loss of energy in the ultrasonic wave. This phenomena can be seen as a reduction of amplitude of the wave. The main factors that effect the amplitude and waveform of the ultrasonic wave are the ultrasonic beam spreading, energy absorption, dispersion, transmission at interfaces, scattering by inclusions and defects, Doppler effect and so on [43]. The ultrasonic attenuation can be quantified by the attenuation coefficient , which is defined by the following equation:

$$A = A_0 \cdot e^{-\alpha x} \tag{2.7}$$

Where A is the peak amplitude of the wave at a propagation distance x and A_0 is the initial peak amplitude.

The attenuation coefficient is experimentally determined from the variation of the peak amplitude with the propagation distance, and it can be given in decibel per metre (dB/m) or in neper per metre (Np/m). In general, this coefficient is highly dependant on frequency. Since this frequency dependence reflects the microstructure of the materials, it can be used for characterizing microscopic material properties relating to chemical reactions or mechanical processes.

Display terminology

During the course of this work, some terms will be used frequently in order to refer to the different views and displays provided by the UT equipment. Those being the following:

- **A-scan**: A data presentation method where signal amplitude is plotted along the y-axis versus time on the x-axis. The horizontal distance between any two signals represents the material distance between the two conditions causing the signals;
- **B-scan**: Produces a two-dimensional view of a cross-sectional plane through the test object (figure 2.15 a)). The horizontal sweep is proportional to the distance along the test object and the vertical sweep is proportional to depth, showing the front and back surfaces and discontinuities between them;
- **C-scan**: Refers to the image produced when the collected data is plotted on a plan view of the component (figure 2.15 b)). It is the image of the results showing a cross-section of the test object parallel to the scanning surface. This scan often shows a combination of measurements obtained through the whole thickness of the part;

- **D-scan**: Image of the results showing a cross-section of the test object perpendicular to the scanning surface and perpendicular to the projection of the beam axis on the scanning surface (figure 2.15 c)). The D-scan view is perpendicular to both the C-scan and the B-scan. However, like the C-scan, this usually shows UT data collected through the whole or part of the inspection volume.

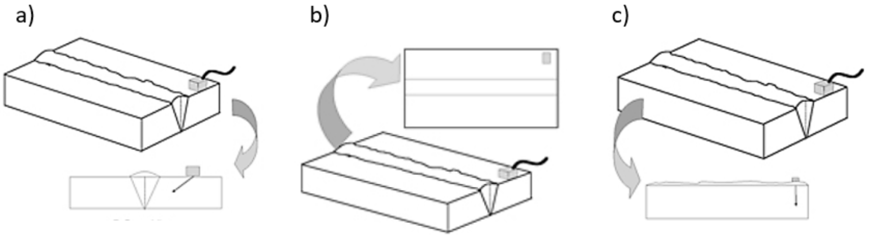

Figure 2.15: UT result displays [47]: a) B-scan; b) C-scan; c) D-scan.

Advanced UT: Phased array

A phased array transducer consists in multiple elements, each of which is analogous to a single element transducer, capable of emitting and receiving ultrasonic waves. By controlling the pulsed time of the elements, the beam generated by the array can be electronically focused and steered . This flexibility is one of the reasons that phased arrays are becoming more commonly used in ultrasonic NDT [48].

Phased array UT (PAUT) features a computer controlled amplitude and delay law for each individual element of the multi-element probe. These elements are pulsed in such a way that multiple beam components combine with each other and form a single wave front traveling in the desired direction, as illustrated in figure 2.16. The excitation of the several elements allows one to generate an ultrasonic focused beam, as well as modifying its angle, focal distance and focal spot size by means of software. The sweeping beam can detect misoriented cracks that are located away from the beam axis.

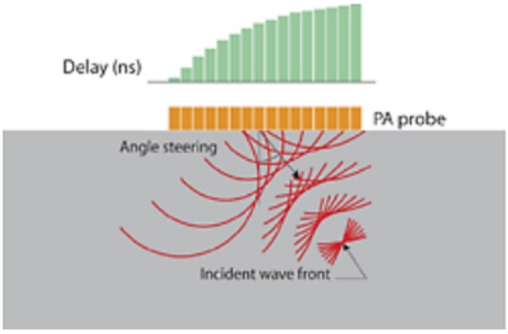

Figure 2.16: Example of angled beam generated by flat probe by means of variable delay [47].

The probe elements can be arranged in several geometries: linear array, annular array, circular matrix or other more complex geometries. They can be used in direct contact with the test piece, with a wedge as an angle beam assembly or for immersion with sound coupling through a water path. Through software processing it is possible to conduct a linear scan, varying the sequence of pulsed elements from a fixed angle, or a sectorial scan, in which the desired area is inspected through different angles.

Lopez et al. [4] studied the effectiveness of phased array ultrasonic testing to detect defects in WAAM aluminium parts. In this study the probes were able to surpass the challenges led by the surface waviness for a maximum of 89.6 µm. This validates the applicability of PAUT techniques for WAAM inspection as defects were successfully characterized in both size and distance to the surface. The feasibility of using this method in WAAM steel samples while accommodating waviness will be studied on chapter 5.

Chapter 3

Manufacture and characterization of samples

With the purpose of studying the implementation of EC and UT techniques to large WAAM steel parts, this chapter aims to detail the steps needed for fabricating the samples to be inspected in the further chapters. To do so, a initial optimization of the welding parameters was conducted, and the originated samples were characterized in terms of structural integrity (i.e presence of defects) and surface waviness.

3.1 Production setup

The WAAM steel samples were produced at Instituto Superior Técnico's facilities using the following equipment listed on table 3.1.

Table 3.1: Laboratory equipment used for the production of samples.

Equipment	**Specifications**
Robot system	Kuka 6-axis
Welding equipment	Fronius CMT VR 7000
Welding wire consumable	AWS A5.18 ER70S-6 $\oslash = 1.2$ mm
Substrate plates	DIN 2391 ST 52 steel
Clamping system	Steel table clamps
Shielding gas	18% CO2 + 82% Argon

The welding torch attached to the Kuka robot was kept perpendicular to the substrate, as seen in figure 3.1, meaning that the relative motion of the robot comprehended only half of it's degrees of freedom (XYZ) ignoring the three rotation axis (A1, A2, A3) in order to simplify the tool path and programming involved, which was done using Autodesk PowerMill.

After the robot preparation, it was necessary to set the welding parameters in the Fronius CMT machine. The first step consisted on using the controller to choose the most adequate synergic line. As explained in section 2.3.1, a correct selection of the material curve is crucial for obtaining the best results when welding, therefore, the synergic line for g3si1 wire (which is the EN ISO 14341-A norm equivalent to the AWS A5.18 ER70S-6 wire electrode being used) was chosen.

After selecting the curve, the CMT machine suggested two shielding gas options. In this case, a mixture of 18% CO2 and 82% Argon was selected, as [20] observed that the welding drops were smaller with the reduction of CO2. The selection of a proper gas is decisive not only for the process stability but also for improving the surface finish and spatters reduction. The gas flow rate was kept constant throughout the experiments, and equal to 20 l/min.

(a) Kuka 6-axis robot.

(b) Fronius VR 7000-CMT machine.

Figure 3.1: Welding equipment.

For the substrate, a ST52 steel plate with σ_{UTS} = [510, 630] MPa was used. In WAAAM, it is important that the mechanical properties of the base material are well suited for the welding wire being utilized. Prado-Cerqueira et al. [20] recommends that the base material should present a minimum σ_{UTS} = [400,480] MPa, but considering the ER70S-6 wire, a range between 400 and 550 MPa is deemed suitable. For values higher than this interval, which was the case, the homogeneity of the mechanical behaviour is not guaranteed. Nevertheless, this shouldn't present a problem in the context of this thesis, because the objective is to inspect the upper layers of the samples which means that the mechanical bonding between the first layers and the substrate is out of scope for this particular scheme. When the primary objective is to actually manufacture a part to be mechanically loaded *a posteriori*, it is then advised to use a proper substrate compatible with the wire.

Regarding the torch setup showed in figure 3.2, the stick-out (distance from the end of the nozzle to the end of the wire) was approximately 8 mm while the nozzle-to-work was kept at 10 mm in all experiments. In order to keep this last parameter constant, the robot path had to be programmed in a way that the torch would move 2 mm in the vertical Z direction after the first bead, and then increment 0.5 mm in the following layers so as to compensate the higher heat input that develops within each cycle, increasing the layer height. Without doing so, the nozzle-to-work distance would decrease significantly in the taller WAAM walls and end up damaging the torch.

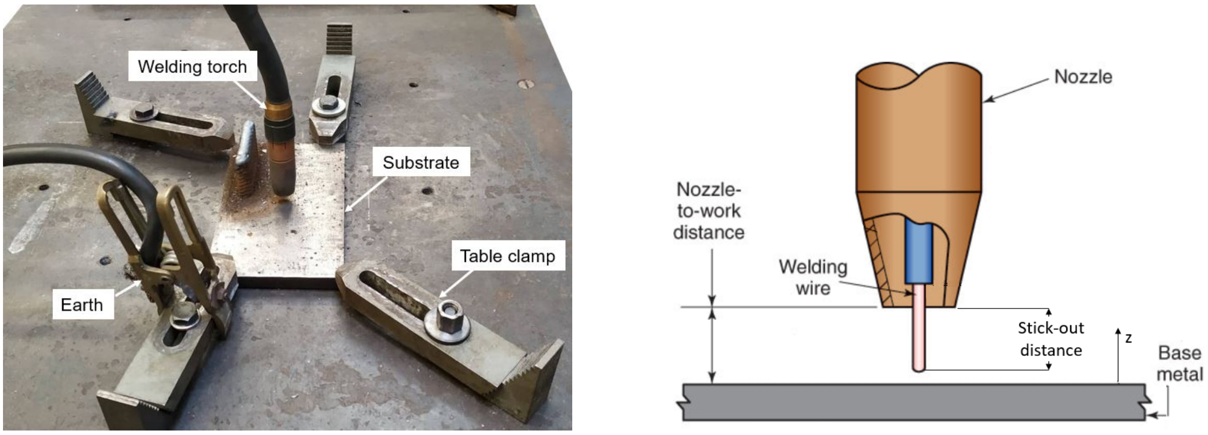

(a) Clamping system.

(b) Arc welding relevant distances, adapted from [49].

Figure 3.2: Torch setup and relevant parameters.

3.2 Process parameters optimization

As expressed in the beginning of this chapter, the following optimization had the objective of producing samples with good structural integrity to be inspected by the selected technologies. Due to the size limitations of both the ECT and UT techniques, it was important to guarantee a large range of sample widths. This was possible through numerous iterations and parameter combinations to provide the requested deposit width. Moreover, for the future of WAAM, a flexible way of controlling the geometry is desirable to automate the process and to minimise material waste. Also with inspection in mind, minimum waviness was one of the focuses for this optimization because of its relevance in increasing the signal-to-noise ratio (SNR) and in improving accuracy when inspecting.

The first step consisted on checking the repeatability of the experiments. To do so, three samples with the same welding parameters, number of layers and cooling time, were deposited next to each other. It was verified that the samples were similar in terms of geometry, with a maximum variation of 0.2 mm in height and 0.1 mm in width.

Subsequently, it was necessary to establish the waiting time between layers. Rodrigues et al. [45] studies on the effect of thermal cycles on microstructure and mechanical properties of HSLA steel have shown that [2,5] minutes were enough to achieve a temperature between 800 and 500 $^{\circ}C$ (which is known to be critical as it controls the solid-state transformations of the material), depending on the accumulated heat input of the sample. For this reason, the cooling time was kept at 3 minutes for most samples, except for the tensile test specimens of chapter 5.3.2, where 4 minutes were selected as higher heat accumulation was being promoted by the high number of deposited layers.

The systematic procedure of this experimental work was conducted by varying the WFS and WFS/TS ratio, as explained in the literature review. The addition of this last term serves to control the added material per unit length. During the preliminary experiments for determining the process window capabilities, the Fronius CMT welding machine would only allow a range of WFS = [2, 8.3] m/min for the G3si1 material. When the first attempt of the experiment was made for the minimum value of WFS = 2 m/min, the electric arc would not ignite. After further attempts, it was concluded that only values above 3 m/min would start the arc. On the other hand, for a WFS above 7 m/min the arc would be abnormally unstable promoting spatters and hindering the surface quality of the samples. In consequence, WFS = [3, 7] m/min was the actual useful range for this parameter. Also regarding the WFS, it is also worth mentioning that the CMT process involves the precise control of this parameter by the power supply to keep the arc length constant and independent of surface and stick-out changes. This process control creates a difference between the adjusted and real (measured) wire feed speed. This means that, according to Ali et al. [50], the real WFS in CMT-process is 20–32% less than the adjusted feed speed.

One of the first objectives of this experiental work was to evaluate the influence of the WFS and WFS/TS ratio in the geometry and texture of the samples. A first study was done by varying the material per unit length (WFS/TS ration), keeping the WFS constant. The process capabilities for WFS = 7 m/min, 6 layers and 3 minutes of cooling time are plotted in figure 3.3.

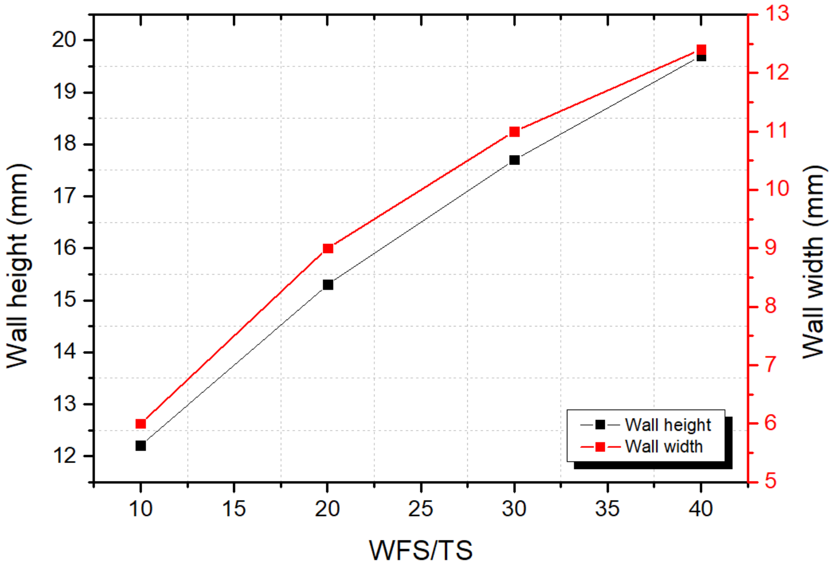

Figure 3.3: Racio influence on width and height for constant WFS = 7 m/min.

The graph shows that for constant WFS, higher ratios (i.e lower TS) promoted an increase in wall width. This is due to the fact that TS is inversely proportional to the heat input, as shown by equation 3.1, which means that alower TS results in higher heath inputs, which consequently promotes higher wall widths as Martina [12] verified for TIG based WAAM.

$$HI = \frac{V\ \text{Current}}{TS} \tag{3.1}$$

This implies that heat input alone can explain most of the variations seen in the experimental data for the wall width, which consequently makes it highly dependant on the current.

As for the total wall height, its dependence on the heat input is more complex. According to Martina [12], the layer height is related to the WFS/TS ratio and is also dependent of the heat input. Hence, the layer height behaviour will depend on which is increasing more: if the ratio itself or the heat input. According to the experimental results, it appears to be the first case, as the total wall height was increasingly higher and more wire was being deposited per unit of time.

In terms of process capability, the chosen parameters permitted the production of samples with wall widths ranging from 6.5 to 12.4 mm and the total wall heights from 11.7 to 19.7 mm for 6 layers.

As for the surface waviness, both the WFS and WFS/TS ratio had a crucial role on the texture of the samples produced, as summarized in figure 3.4. All samples were manufactured with 6 layers and 3 minutes waiting time. For combinations that stand on the red lines of the figure, the superficial quality of the walls is not guaranteed.

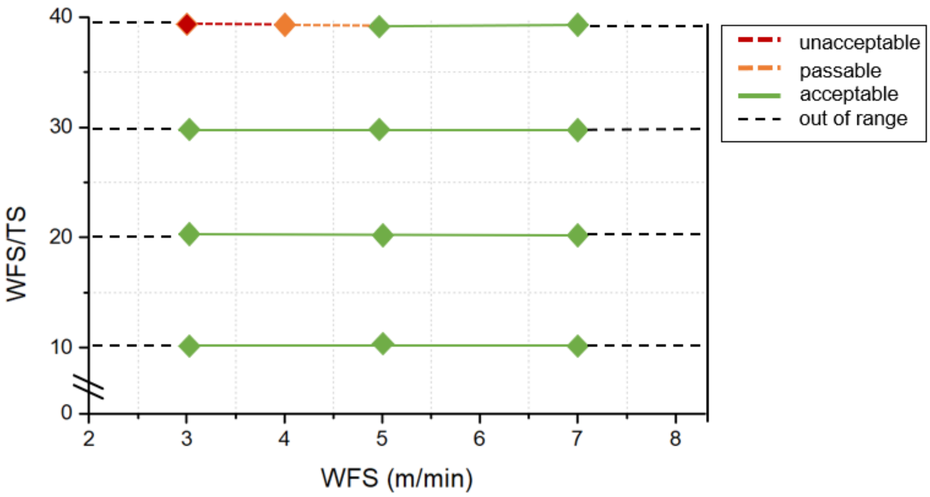

Figure 3.4: Working envelop of CMT deposition. Surface texture and bead shape acceptance.

For WFS/TS = [10, 30], the surface quality was acceptable for the whole WFS range. On the other hand, for the highest ratio tested combined with the lowest WFS value, the surface texture was the worse compared with it's counterparts. Coincidentally, this sample was fabricated with the lowest TS of all experiments, 2.9 mm/s. This mean that theoretically, this should have been the sample with highest heat input.

It is important to note that the substrate plates dimensions were different throughout, affecting the quantity of heat transferred by conduction from the plates to the table. Additionally, when various samples were made on the same substrate, the initial temperature of each one would vary i.e the first sample would be deposited with the substrate at room temperature and the following ones wouldn't, which is not ideal. Nevertheless, if the focus was to actually manufacture large steel parts instead of WAAM walls for mainly inspection purposes, it would be advisable to pre-heat the substrate and/or using a cooling plate as [50] and [24] suggest.

3.3 Preliminary visual inspection and radiographic testing

Visual testing (VT) is the oldest and most common NDT technique and it is typically the first step before any inspection process. In the prior subchapter, four extreme cases were found, which corresponded to the WFS/TS and WFS limits of the working envelop. These were called samples A B C and D and their parameters are recalled on table 3.2.

First and foremost, sample D failed the preliminary visual inspection as it fell on the red region of the last figure. Then, samples A, B and C which presented acceptable surface waviness and bead shapes were took to ISQ NDT Lab facilities to undergo a radiographic inspection. This technique is commonly used due to the capabilities of rapidly mapping internal defects that the VT isn't able to detect, such as lack of fusion, inclusions and porosity.

The equipment used for inspecting the steel samples was the Andrex Micro-focus 300kV, portable-ray system. The time of exposure had to be adjusted to each sample's thickness, as presented on table 3.2.

Table 3.2: Visual inspection results and X-ray testing parameters.

Sample	WFS/TS	WFS [m/min]	Visual inspection	Time of exposure [s]
A	10	3	✓	30
B	10	7	✓	30
C	40	7	✓	120
D	40	3	Failed	N.A

The results of the X-ray inspection are shown in figure 3.5, along with the parameters that were common to all samples. An 10 FE EN image quality indicator (IQI) was used along with type D4 film.

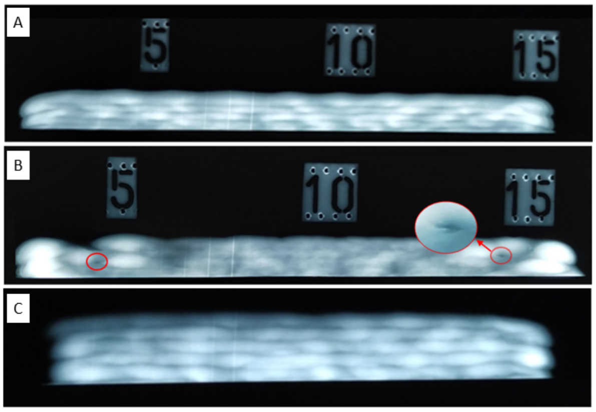

(a)

Parameter	Value
Source-film distance	505 mm
Tube current	4 mA
Tube voltage	160 KV

(b)

Figure 3.5: X-ray testing results and common parameters used.

As observed, in both samples A and C no porosity, lack of fusion ou inclusion defects were detected. On the other hand, sample B showed two abnormal zones (red circles in the figure) which resemble a typical lack of fusion defect. While sample D had the lowest TS, sample B had the highest of all experiments: TS = 11.7 mm/s. This means that, following previously used logic, sample B had the lowest heat input which consequently hindered the samples' structural integrity.

All things considered, it can be said that for obtaining the best structural and surface quality in a CMT WAAM deposition, there has to be a compromise between the WFS/TS and WFS selected parameters in order to keep the heat input at an optimal level.

3.4 Influence of the deposition strategy

Although most samples had an acceptable texture to the unaided eye, it is of great interest to diminish the waviness as much as possible in order to avoid the extra step of machining the walls to benefit the EC and UT inspection. With that objective in mind, the deposition strategy was optimized to minimize surface waviness without compromising the sample's microstructural integrity.

All samples mentioned in the previous section were produced using an oscillation deposition strategy where the tool travelled a linear path, as exemplified in figure 3.6. According to Ermakova et al. [51], "oscillation patterns offer several advantages compared to the parallel, such as flexibility of building various wall widths without continuous change of weld parameters. Therefore, it provides more accurate control of wall thickness". Also, oscillation strategy reduces the probability of lack of fusion defects, since this process is warmer when compared to the parallel deposition.

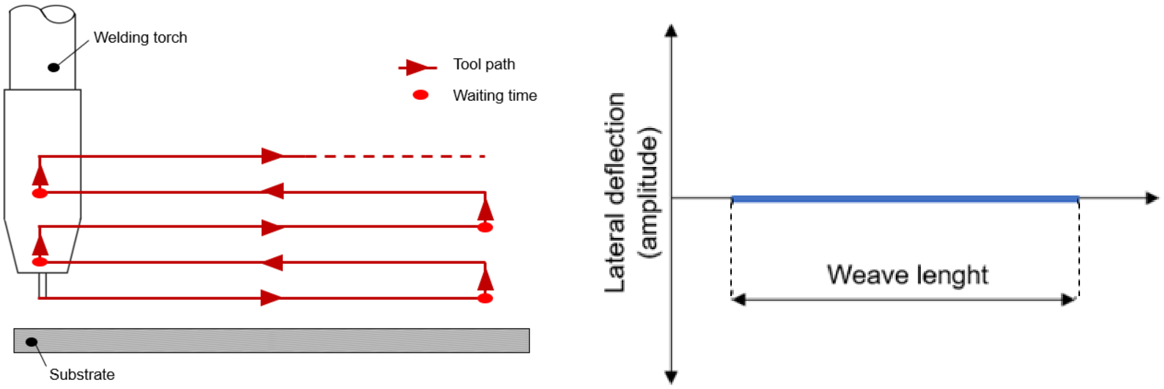

(a) Linear tool path.

(b) Linear depositon parameters.

Figure 3.6: Oscillation deposition strategy.

With waviness improvement in mind, a triangular weaving deposition strategy was attempted. As shown in figure 3.7, when a leading line is set, the trajectory of the welding torch swings along the guiding line, generating a wide weld bead. One of the objectives of this section was to further investigate on the influence of the weaving parameters on the surface quality, as it follows.

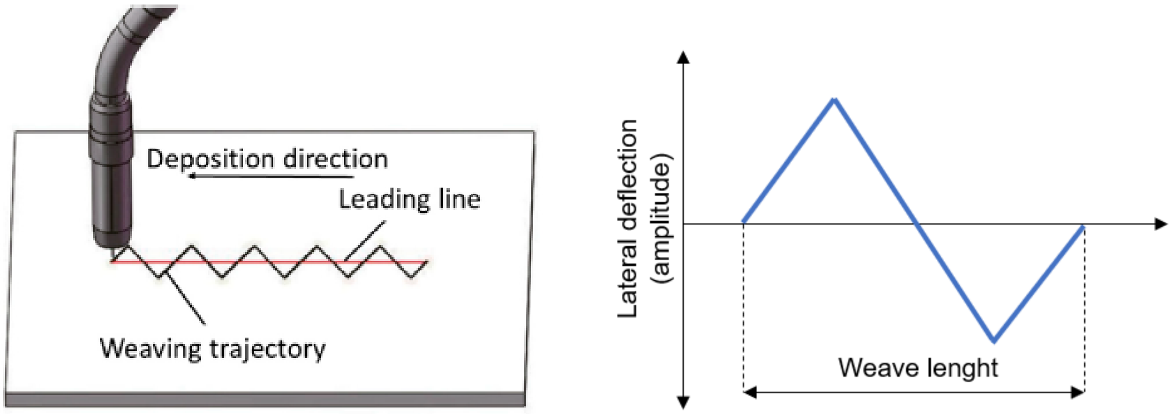

(a) Weaving deposition strategy [2]. (b) Triangular weaving parameters.

Figure 3.7: Triangular weaving pattern deposition.

3.4.1 Waviness profile

In the robot programming, there were mainly two parameters for the weaving motion of the torch, namely, amplitude (W_a) and weave length (W_l). Increasing these variables leads to a more "spread" bead as increasing the W_a transversely stretches the welding pool while increasing the W_l tends to extend it. This leads to a flatter welding bead with a decreased contact angle (figure 3.8). In fact, when using weaving, the sample's width ceases to be only a function of the heat input alone as mentioned previously, and begins to account for the W_a.

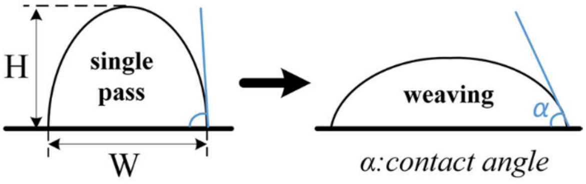

Figure 3.8: Weaving influence on the contact angle [52].

The purpose of this subchapter was to understand if manipulating the weaving parameters to promote a wider and flatter bead would improve the surface waviness. Some preliminary tests were made ir order to comprehend the W_a and W_l relation. When the TS along the leading line is set, the speed along the weaving trajectory is calculated by the program. This means that for the same leading TS, a decrease in length will be compensated by an increase in velocity along the weaving path itself, causing the torch to vibrate compromising the surface texture. For this reason, a compromise must be done: if a higher value of W_a is used, the W_l should also be increased accordingly.

For a first study, it was decided to fix the W_l to 4 mm and elongate the molten pool only by varying the W_a. Therefore, two samples were produced with the same welding parameters as sample C from the last subchapter but different W_a. Because the sample with the same welding parameters but fabricated by an oscillation deposition strategy was approximately 13 mm wide, two approaches were made regarding the W_a selection, both illustrated in figure 3.9 a): Sample 1 had W_a = 6 mm in order to "accompain" the original width of the same sample without weaving. Sample 2 had a smaller value, W_a = 3 mm. The hypothesis was that a larger W_a would produce a flatter bead, improving surface waviness.

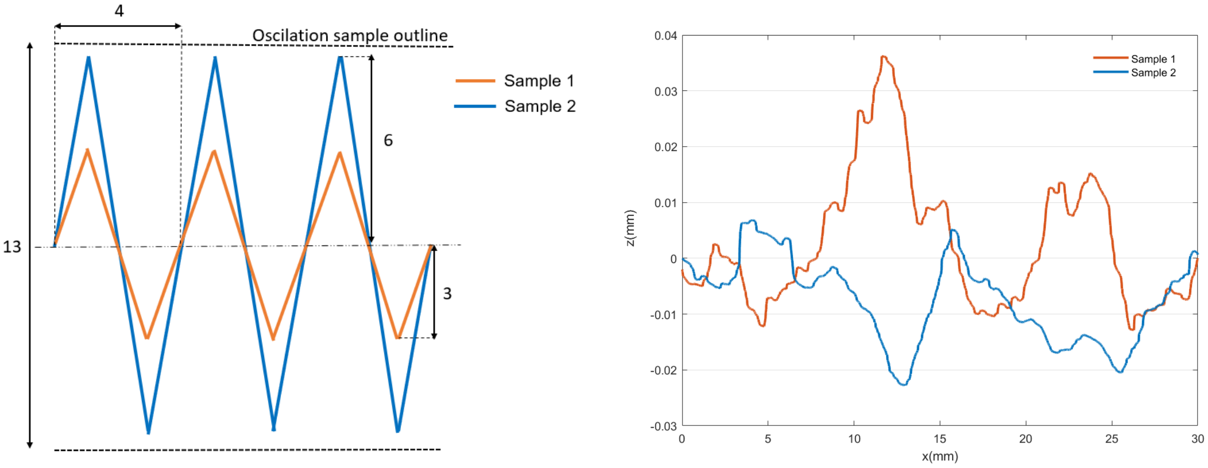

(a) Weaving parameters lustration. Dimensions in mm.

(b) Filtered waviness results.

Figure 3.9: Weaving amplitude influence on waviness.

In order to study the waviness, a *Stil Initial* chromatic confocal sensor was used to measure the δ_Z in the building direction on a 30 mm linear path along the leading direction x .

The acquired data was actually a measure of the surface texture which is the composition of roughness plus waviness. Because a 1-D median filter on MATLAB was applied to the Z values to reduce the noisesome results, the filter also reduced part of the roughness variations, which means that the graphs obtained are, in reality, an approximation of the waviness profile.

By observing figure 3.9 it is possible to confirm the initial hypothesis as the waviness was significantly reduced by the use of a higher W_a. Sample 1 made had a maximum Z value of $\approx$ 36 µm while sample 2 had a maximum absolute value of $\approx$ 23 µm.

After concluding that better surface waviness was obtained for a total amplitude variation closer to original width of the sample fabricated with oscillation, the same logic was used to produce thinner samples with the objective of being used on the existing customized eddy current probes, which demanded smaller sample widths. It was also important to understand if the logic above would apply when other welding parameters were used. Sample A from the last subchapter was $\approx$ 7 mm wide when a oscillation deposition strategy was used, therefore, W_a = 3 mm was selected in order to follow the same logic represented in figure 3.9 a) of accompanying the original oscillation width. The W_l was reduced accordingly. Figure 3.10 presents the filtered results for both the thinner sample a) and the largest b) comparing the weaving and oscillation results while using the same welding parameters.

These results allow to conclude that the triangular weaving deposition strategy was indeed beneficial for the waviness when compared to it's oscillation counterpart. This was verified both for thinner samples fabricated with a low WFS and WFS/TS ratio and wider samples with higher WFS and WFS/TS. However, it was also evident that the use of weaving was more beneficial in the first case, promoting a maximum value under 10 µm. According to [53], this can be explained by the fact that the increase of WFS tends to decrease surface quality due to the combining effects of the layer height and arc force.

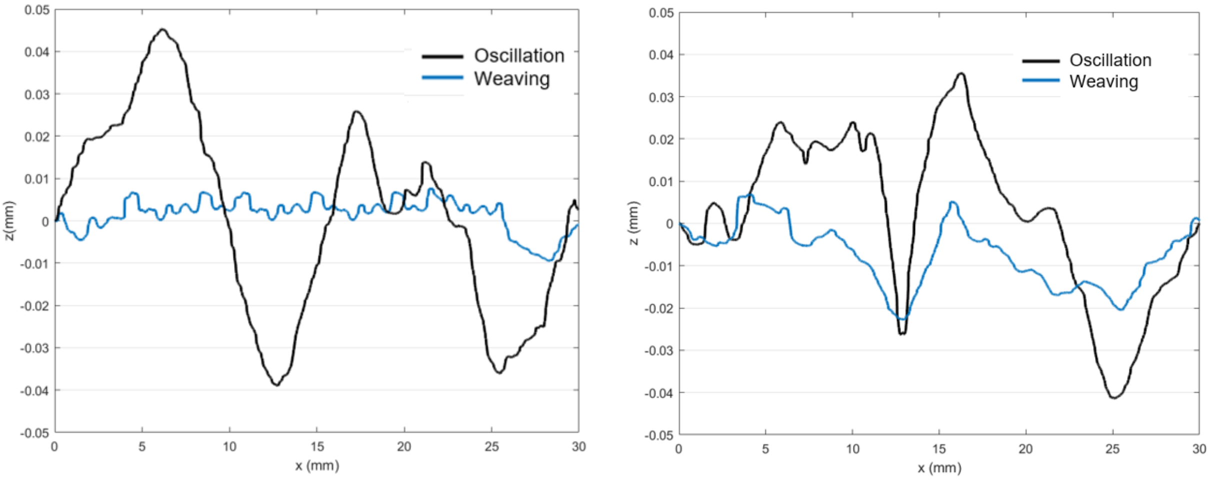

(a) Welding parameters: WFS=3 m/min and WFS/TS = 10. Weaving parameters: W_a = 3 mm and W_l = 2 mm

(b) Welding parameters: WFS=7 m/min, WFS/TS = 40. Weaving parameters: W_a = 6 mm and W_l = 4 mm

Figure 3.10: Weaving influence for different welding parameters.

Therefore, samples fabricated with a smaller WFS value will tend to perform better regarding waviness.

With the successful optimization of the process parameters with the objecting of benefiting inspection, a microstructural analysis was followed in order to understand if this strategy was detrimental to the samples when comparing to the oscillation counterparts.

3.4.2 Microstructure

For this study, two samples were used, each produced with the same welding parameters as sample C from the last section, as it presented no signs of superficial and internal defects both by visual and X-ray inspection. The samples differed on the deposition strategy used: oscillation and weaving.

In order to analyse the microstructure, a traversal section of both samples was removed and resin-wrapped before polishing. After that, 2% Nital was used as contrast. The macro and microstructure results are presented in figure 3.11.

As can be observed on the macros, the weaving strategy tends to change the bead shape from tall and narrow to short and wide. This is done through physical dragging the weld pool which consequently elongates it and as a result, the bead width increases. Regarding the microstructures, no defects were detected. Both samples share identical microconstituents on equivalent portions and similar grain size. On the top area #1, acicular ferrite (AF) and grain boundary ferrite (GF) structures can be seen. On the middle and bottom portions #2 and #3, the structure is resonant to the one found in carbon steel multipass welds, where weld metal which has been reheated by a subsequent weld pass has a rapid thermal cycle, resulting in very fine ferritic transformations. Such microstructure is normally associated with very good toughness.

In conclusion, the triangular weaving deposition strategy proved itself to be beneficial to the surface waviness of the samples when compared to oscillation, while maintaining structural integrity with no defects and similar microconstituents.

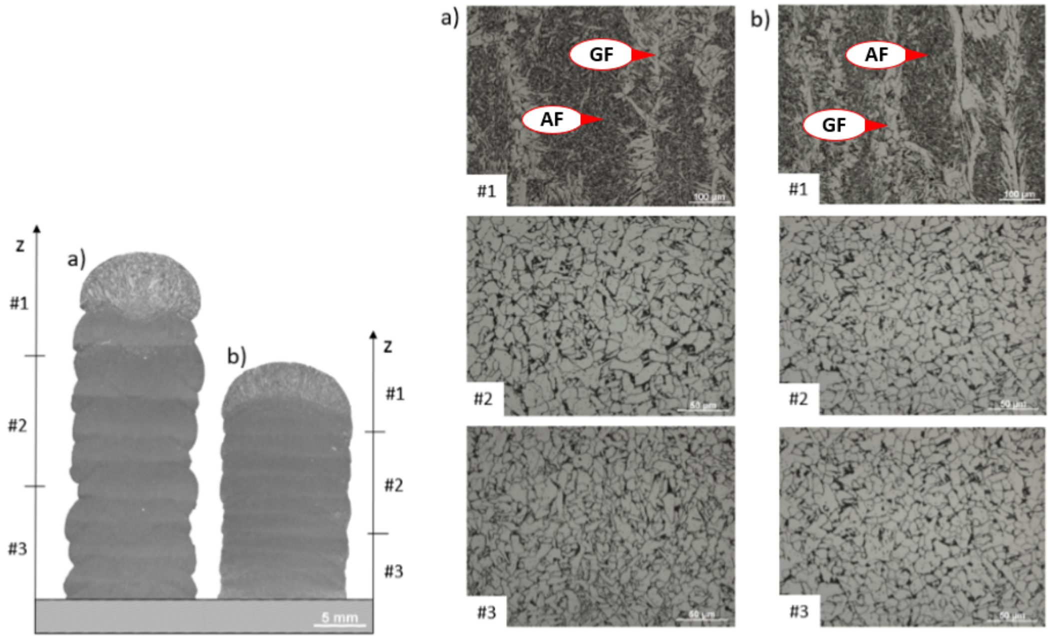

Figure 3.11: Macro and microstructure results for a) oscillation, b) weaving.

Chapter 4

Eddy Current Testing

4.1 Evaluation of existing ECT IOnic probes in steel

The main goal of this chapter is to study the in-line detection of defects in steel WAAM samples using Eddy Current Testing (ECT). As explained on section 2.4.3, the development of customized EC IOnic probes [5] proved to surpass the limitations of its commercial predecessors when considering the inspection of aluminium WAAM samples. However, steels are the most widely utilized metal family in modern manufacturing and are now being applied across multiple AM processes and in perhaps the widest variety of alloys compared to any other material group also being additively processed today. Although these preliminary results in aluminium represented an important step towards the development of NDT systems for WAAM, its important to access the capabilities of this inspection technique in steel and other ferromagnetic materials.

As discussed in the state of the art, the eddy currents that flow in the metallic structure are sensitive to several factors, such as the material properties (electrical conductivity and magnetic permeability), test frequency, lift-off effect, edge effect and the dimensions of the crack. The flow of eddy currents in a conductor is maximum at the material surface and it is attenuated with increasing depth. However, for low magnetic permeability as it is the case for most non-ferromagnetic materials such as aluminium, the eddy currents achieve deeper penetration.

Materials which possess a high relative permeability value, $\mu_r \gg 1$, are called ferromagnetic materials because of their own innate ability to exhibit magnetic effects. In contrast to other substances, ferromagnetic materials are magnetized easily and in strong magnetic fields the magnetization does not return to its original value - hysteresis. In figure 4.1 it is shown the standard depth of penetration, based on equation 2.3, for two different materials: aluminium, considering $\sigma \approx$ 30% IACS and $\mu = 1$ H/m; and mild-steel with $\sigma \approx$ 5% IACS and $\mu = 2000$ H/m .

Although the values of μ and σ used were merely exemples as both can vary depending on several conditions, one can observe that the standard depth of penetration in steel is almost 95% less that in aluminium due to the ferromagnetic characteristics of the first, confirming the importance of the magnetic characteristics for the effectiveness of the ECT method. For this reason, when using ECT on this type of

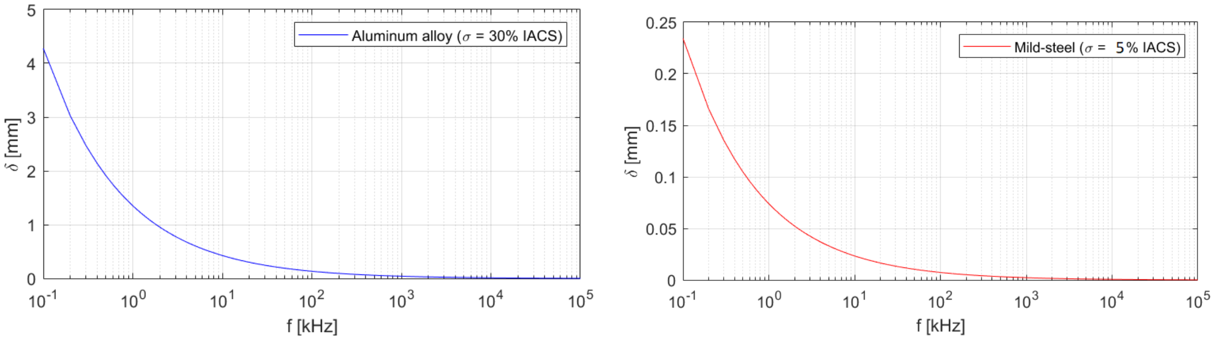

(a) (b)

Figure 4.1: Standard penetration of aluminum (a) and mild-steel (b) in function of the frequency used.

materials, the probes must operate at very low frequencies which requires coils with more windings, ergo larger coils. This results in lower probe resolution, which makes results noisier. Because permeability varies within the material, even if the proper penetration can be achieved in ferrous materials, the level of noise will be high. Moreover, in the particular case of WAAM, each layers surpasses a different thermal cycle and cooling, which means that the magnetic properties of the metal will vary within each layer.

Although it seems challenging to use ECT when inspecting steel considering the previous knowledge, some authors such as [54] and [55] have already successfully implemented different strategies on the method to detected and measure surface cracks in this type of materials. These results greatly motivate further investigation on different ways to overcome the difficulties of ECT in ferromagnetic materials. Furthermore, considering that one WAAM sample layer is about 2.5 mm high, the probes do not have to achieve great levels of penetration in the material for the objective of in-line inspection, which should facilitate the ECT probe development in this case.

With the previous considerations in mind, the first approach of this work was to study if viable results could be achieved when using the past customized EC IOnic probes on steel, since their innovative geometry and *modus operandi* could be enough to surpass the material's limitations.

4.1.1 Numerical modelling comparison: aluminium and steel

Primarily, a comparative study on the behaviour of customized IOnic ECT probes on aluminium and steel was backed-up with a numerical simulation based on finite element analysis (FEA) to solve and illustrate the electromagnetic phenomena of the EC probes. The software used was ANSYS Electronics – Maxwell 3D and its solvers are designed to solve Maxwell's equations 4.1 and 4.2 within the scope of a specific solution type. In this software, the fundamental unit of the finite element is a tetrahedron (foursided pyramid).

$$\oint_L \vec{E} \cdot dl = -\frac{\partial}{\partial t} \iint_S \vec{B} \cdot dS \tag{4.1}$$

Maxwell – Faraday Equation: The voltage induced in a closed loop is proportional to the rate of change of the magnetic flux density on the surface that the loop encloses. $\vec{E}$ is the electric field [V/m] or [N/C] and $\vec{B}$ is the degree of magnetic induction [T] or [(N.s)/(C.m)].

$$\oint_L \vec{H} \cdot dl = \iint_S \left(\vec{J} + \frac{\partial \vec{D}}{\partial t} \right) \cdot dS \tag{4.2}$$

Ampère's circuital law: The magnetic field induced in a closed loop is proportional to the electric current plus the displacement current (rate of change of the electric field) on the surface that the loop encloses. $\vec{H}$ is the magnetic field [A/m], $\vec{J}$ is the electric current density [A/m^2] and $\frac{\partial \vec{D}}{\partial t}$ is the displacement current density [A/m^2].

In previous work, Bento et al. [5] developed the IOnic probe to inspect an aluminium AA 6082-T6 bar. The probe's coils were made of copper and an input current of 1 A and frequency of 2 kHz was used to reach higher penetration depths. The excitation coil had 50 turns and the sensitive coils had 20 turns each (without current as an initial condition) and were wound up in opposite directions. In order to compare the results for different materials, an identical simulation was ran using the same probe, sample geometry and inspection parameters. The difference was that the selected material in this case was steel (from Ansys library) with a bulk conductivity of 5.86 x 10^{-6} s/m and relative permeability of 3000 which means the B-H curve effect was neglected for simplification purposes.

In both simulations, a defect was designed as a rectangular hole composed of air (null electrical conductivity) throughout the width the bar (6 mm in the Y direction), with 2 mm length (X direction) and 1 mm thickness (Z direction). The top of the hole is 4 mm below the surface of the bar. Both bars had some curvature to their surface in order to approximate the model to a typical WAAM surface, while ignoring the texture to simplify the analysis. The results are presented in figure 4.2.

This results provide information on how the currents flow in the surface of the samples for different materials in the same conditions. As expected, the current density J is higher near the excitation coil on both cases.

By observation of figure 4.2 a) it is possible to observe that the EC flow in the aluminium bar is perturbed by the defect. In this case there is high current density near the surface of the material that decreases as soon as EC reach the defect. This simulation result shows that this perturbation on the EC flow would cause an impedance variation on the probe and, therefore, the defect would be detected through ECT.

In contrast, the magnitude of the current decreases substantially in the z direction in the case of the steel bar, as seen in figure 4.2 b). Moreover, the EC don't seem to be be perturbed by the defect and the current from the excitation coil doesn't reach the sensitive coils with as much intensity as the previous example on aluminium, which can be troublesome.

The intent of comparing these simulations was to understand the differences in current density distribution between ferromagnetic and non-ferromagnetic materials in the presence of a defect. In order to fairly assess if viable results can be obtained in steel while using this type of IOnic ECT probe, an experimental evaluation is followed for different kinds of defect morphologies.

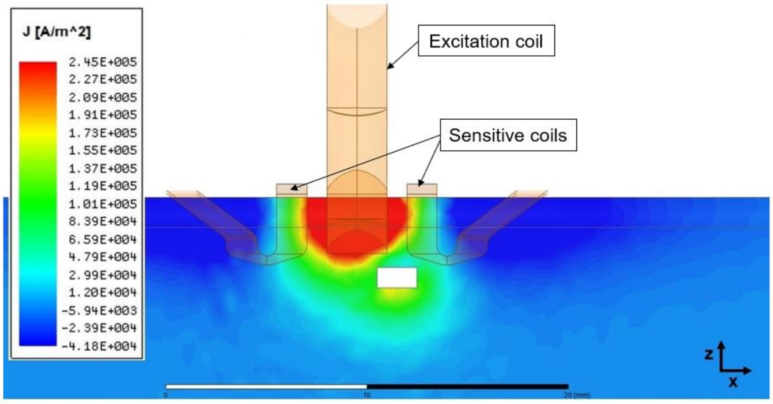

(a) Alluminum bar results from [5], adapted.

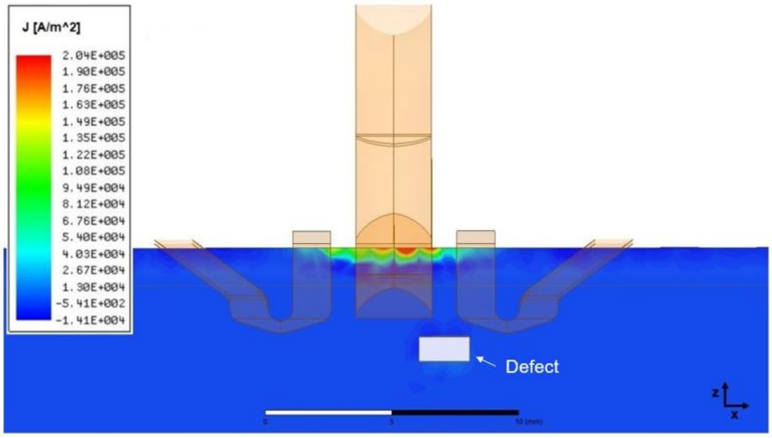

(b) Steel bar results.

Figure 4.2: Magnitude of the current density $\vec{J}$ comparison in the XZ plane for f = 2 kHz.

4.1.2 Detection capabilities of the IOnic probe on steel

Before any experimental analysis with ECT, some external equipment is required in addition to the probes. The experiments were made at FCT - UNIDEMI NDT lab facilities and the equipment used in the present chapter is represented in figure 4.3.

All of the acquired results were treated with the use of a moving average (MA) filter on MATLAB. This is a simple Low Pass FIR (Finite Impulse Response) filter, commonly used for smoothing an array of sampled data/signal. It takes L samples of an input at a time and takes the average of those L-samples producing a single output point.

The first tests were conducted on a steel bar with dimensions 15 x 4 x 0.8 cm. This component was used because of its curvature on the top surface similar to a typical WAAM wall, but without the associated roughness and waviness which would cause unwanted noise in the results. Moreover, this also allowed a more simplified analysis without the dissimilar magnetic proprieties of the different layers. After some preliminary experiments with surface defects, the three different types of customized IOnic probes [5] were put to test on a 3 mm diameter drilled hole, with its top being 2 mm bellow the top surface. The model #3 of the probe was the one that had the best performance i.e the highest SNR, and

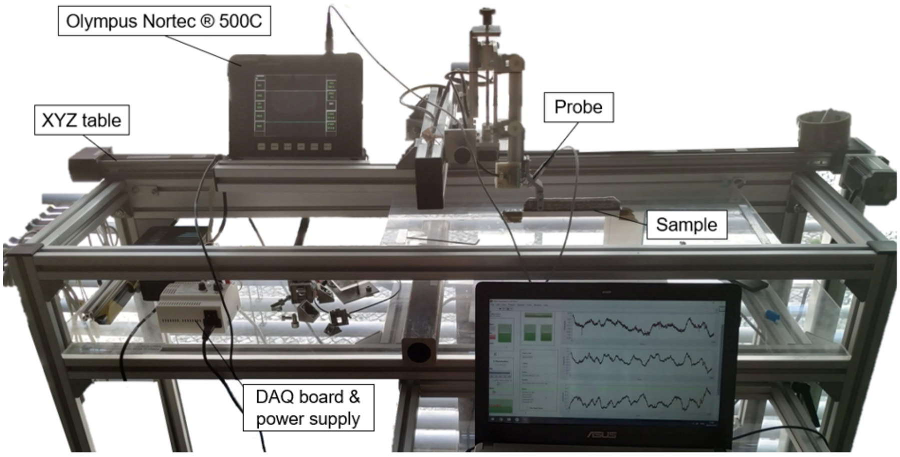

Figure 4.3: ECT laboratory equipment and setup.

its results are illustrated in figure 4.4. As explained in section 2.4.2, the IOnic probe works on differential mode, meaning the resulted signal will show two peaks with symmetric values of impedance variation, instead of only one absolute peak. This is due to the fact that this probe has two sensitive coils winding in opposite directions and therefore the impedance varies based on the difference sensed between those two coils. This is clearly illustrated by the results of the last mentioned figure, as the probe detects the defect using a frequency of 3 kHz.

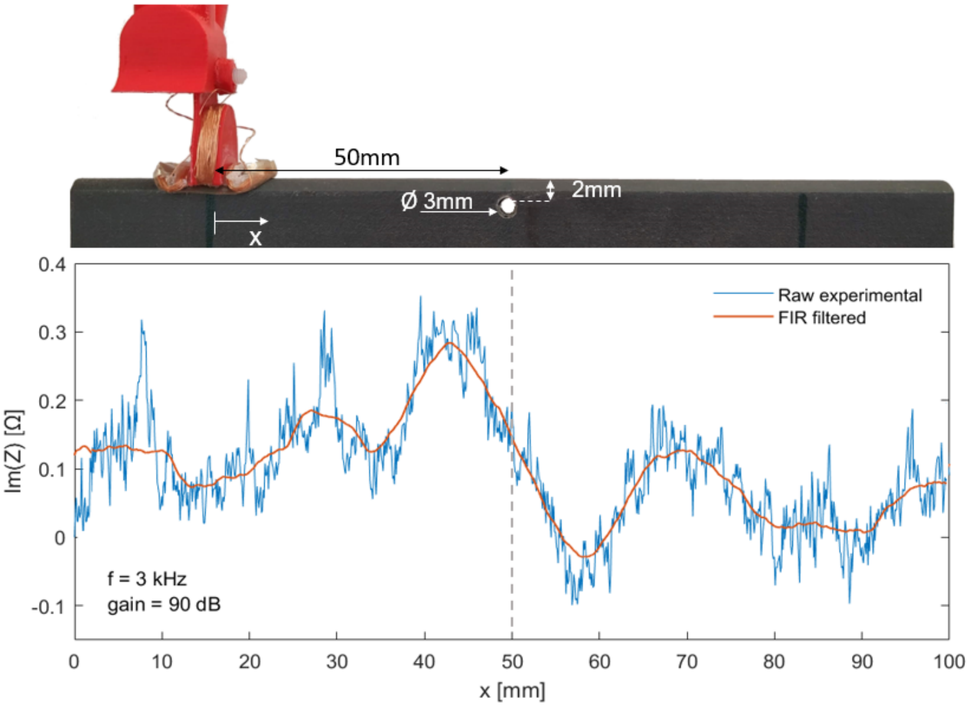

Figure 4.4: Results obtained with the IOnic probe #3 for side drilled 3 mm defect, 2 mm subsurface.

Although the outcome of this experiment was successful, it is important to note that the defect is unrealistically large considering that, in a typical WAAM part, the defects are usually internal and micrometers wide. Moreover, the probe only detected the defect for a narrow frequency range of about

[2-5] KHz as otherwise the results were unacceptable. Even with all the simplifications that come from using a steel bar instead of a real WAAM sample the SNR isn't high enough to prevent mistakes in a realistic inspection scenario, even with the use of the FIR filter.

For the listed reasons, and because the results with this probe weren't as satisfactory as the ones obtained in aluminium [5], it was decided to further investigate on different EC IOnic probe designs and working principles, with the objective of developing a more promising model for the in-line inspection of WAAM steel parts.

4.2 New customized EC probe design

With the purpose of detecting internal defects in WAAM samples and improving the SNR while inspecting ferromagnetic materials: the Sideways Excitation Probe (SEP) was developed. This customized probe was designed under the hypothesis that an higher perturbation of the EC field would be achieved by having two ferrite cored excitation coils, one on each side of the sample, with the winding in the same direction. To test if this was the case, a model was created on ANSYS using the same bar and steel material as the previous example of figure 4.2. In this configuration, the sensitive coils had 40 turns each wound up in opposite directions and the excitation coils had both 200 turns wound up in the same direction around a ferrite core.

The steel part was meshed with 50,000 elements with a maximum length of 30 mm per element. A local mesh refinement was made on the area of interest of the steel part (the central portion, as seen in figure 4.5), as this was the place where the defects were placed. Last but not least, air was used as the surrounding region with an offset of 20% in all directions, which specifies the distance that should be left from the model.

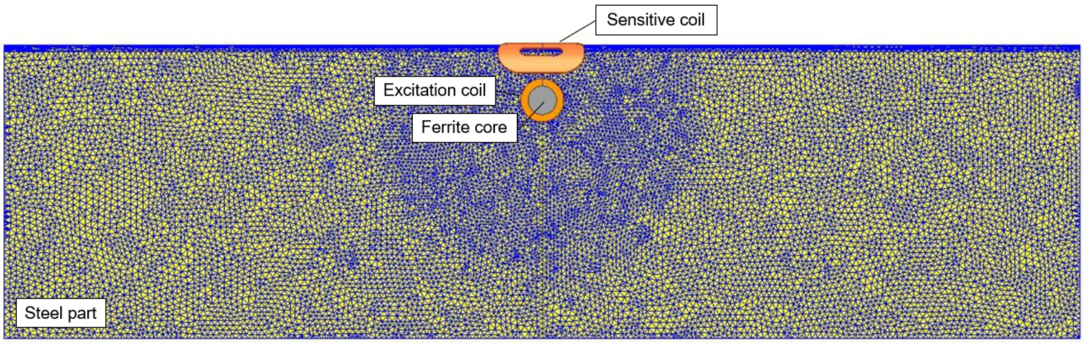

Figure 4.5: Simulation model side view and mesh.

This time, a more challenging defect was designed: a 350 µm x 5 mm (XZ) rectangle that went through all the sample's width in the y direction. The results of this simulation for a frequency of 1 kHz are shown in figure 4.6.

One can observe that the current density is focused all around the laterals and the top of the sample. The defect has clearly perturbed the EC flow as expected since this probe configuration concentrates the EC on the laterals and the defect goes through the samples' entire width. However, the current

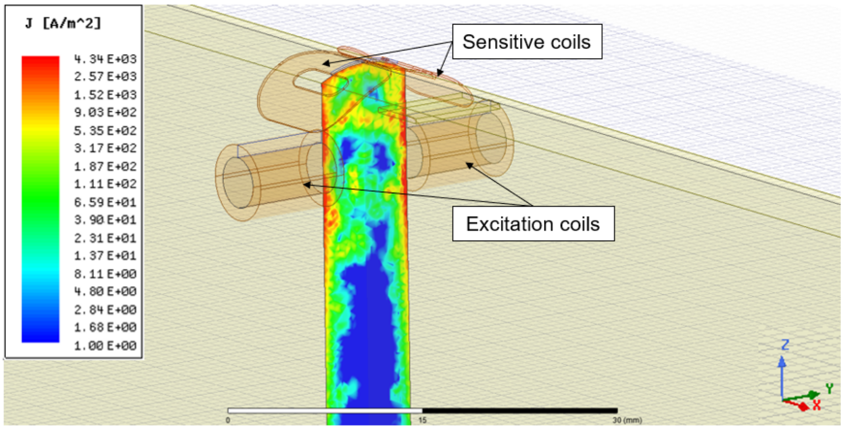

(a) Steel bar without defect.

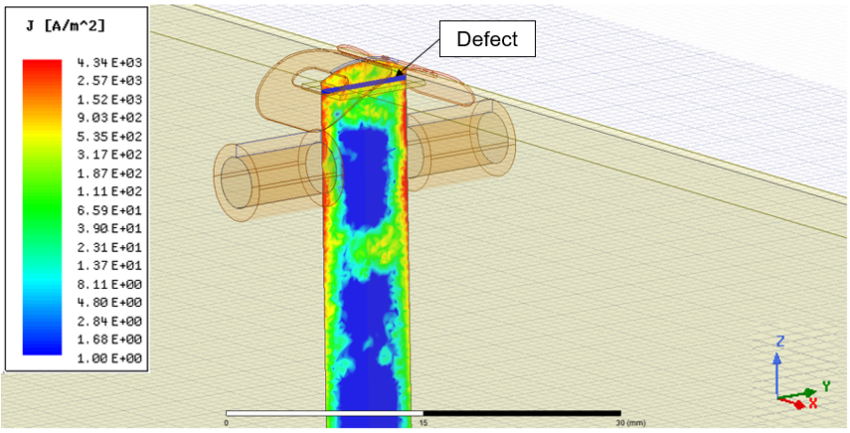

(b) Steel bar with 350 µm x 5 mm (XZ) rectangular defect through widht.

Figure 4.6: The magnitude of the component Y of the field $\vec{J}$ in the XZ plane for SEP probe using f = 1 kHz.

density decreases considerably on the sample's central region, which means that the capabilities of the probe to detect internal defects can be compromised.

It is possible to infer that this probe configuration is more promising for the detection of defects compared to the IOnic model due to the fact that the current density is distributed throughout a larger area of the sample. Not only that, but the current reaches the sensitive coils with reasonable intensity, which was not the case with its predecessor as seen previosly.

4.2.1 Experimental validation of SEP probe

Due to the promising simulation results, a prototype of the SEP probe was 3D printed in Polylactic Acid (PLA) and the molds for the sensitive coils were made of Polyvinyl Alcohol (PVA), a water-soluble polymer that is dissolved after the sensitive coil winding around the mold is completed. The cores of the excitation coils were made of ferrite cylinders with 4 mm diameter. Two PLA screws were added for the possibility to adapt the gap between the excitation coils to the width of the inspection sample. This also allows to adapt the angle between the excitation and sensitive coils. The final design can be seen in figure 4.7.

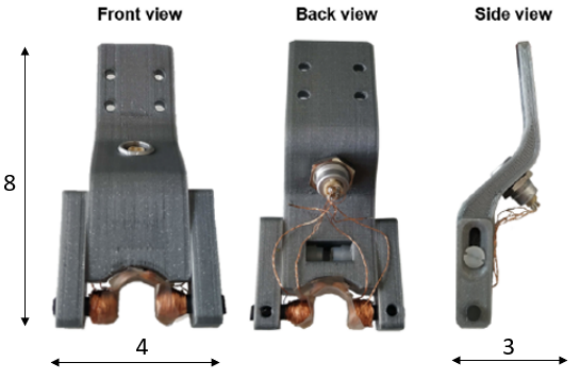

Figure 4.7: SEP probe final design. Dimensions in cm.

Similar to the previous simulation, the sensitive coils were 40 turns each wound up in opposite directions and the excitation coils had both 200 turns wound up in the same direction.

Using the SEP probes it is expected that a defect is signalized by only one peak, as they have a reflection absolution configuration, in opposition to the reflection differential configuration of the customized IOnic Probes.

A first experiment was made on the same 3 mm side drilled defect and steel bar from figure 4.2 in order to compare the IOnic #3 and SEP probes. The results are shown in figure 4.8. Although they are being compared using different frequencies, this outcome serves to show that for the same defect, the best achievable result (for the range of frequencies tested) using the SEP probe had a significantly more accentuated impedance variation while over the defect at x = 50 mm, compared to the IOnic #3 model. Therefore, this probe configuration appears to is clearly an improvement on its IOnic predecessor regarding defect detectability.

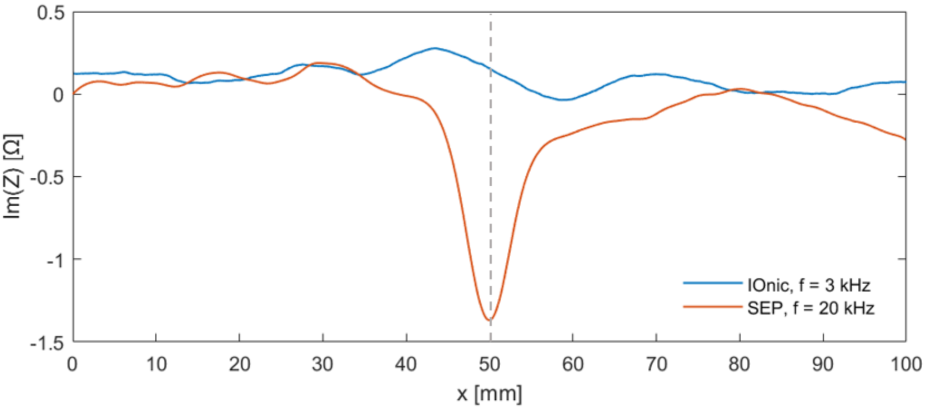

Figure 4.8: Best results from IOnic #3 and SEP probes for a side drilled 3 mm defect, 2 mm subsurface, on a steel bar.

Secondly, it was important for the scope of the project in which this thesis is enrolled, to test the ECT probes on more realistic defects than the ones previously inspected, and on actual WAAM steel samples instead of bars. For this reason, a WAAM wall was fabricated using the triangular weaving deposition strategy that was previously optimized to benefit inspection. The welding and weaving parameters were identical as the ones seen on chapter 3.4.1 figure 3.10 a) as this combination was the less wavy and had a width compatible with the ECT IOnic probes available at the time. Then, wire electrical discharge machining (WEDM) was used to create a 350 µm x 5 mm slot, same as the defect on the last simulation. The slot's top was 2 mm below the surface of the sample and went throughout all of the wall's width, as shown in figure 4.9.

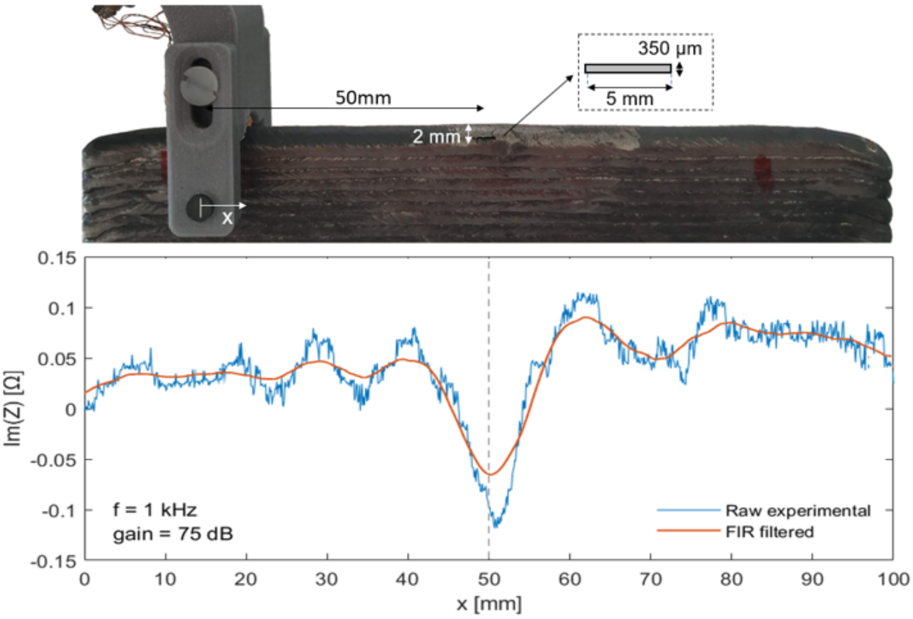

Figure 4.9: ECT results for 350 µm x 5 mm defect.

It can be observed that the probe detects the defect as a peak in the impedance is clear on the x = 50 mm mark. These results were accomplished by using a frequency of 1 kHz and a gain of 75 dB. After this successful result, this probe configuration was challenged by attempting to inspect an internal defect. To do so, the last WEDM defect was closed by welding each side of the WAAM wall using Tungsten Inert Gas (TIG). Chalk powder, a non-conductive material, was placed inside the slot before closing it.

In order to verify if the defect was still present after the welding procedure, radiographic testing was performed. A source-film distance of 700 mm was used, along with W14 wire and an 10 FE EN IQI that can be seen of figure 4.10. After an exposition time of 2 minutes, one can clearly see the defect. The vertical sloth and hole that also appear on the radiography were due to the WEDM procedure, and were previously collapsed with TIG before the last inspection to avoid misinterpreting the results.

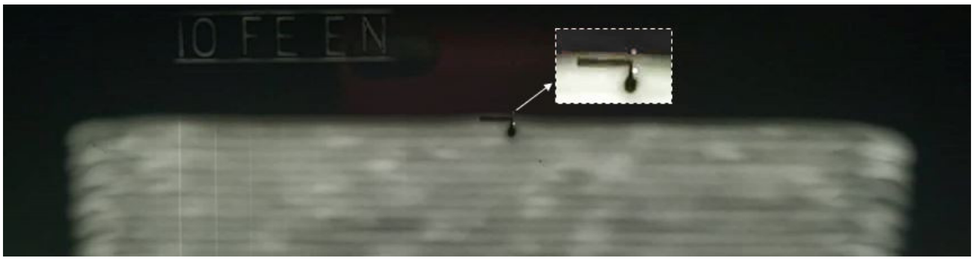

Figure 4.10: Radiographing testing results on WAAM wall with WEDM defect.

This internal defect was then inspected using a wide range of frequencies. The best results were obtained for f = 1 kHz and 82 dB of gain as seen in figure 4.11. Similarly to the "open" defect inspection, the peak can be seen on the x = 50 mm mark but the SNR decreased, as expected. Although the impedance peak indicates a successful detection, the fact that the steel filler material used in the TIG welding wasn't of the same exact steel as the WAAM wall might be influencing the results.

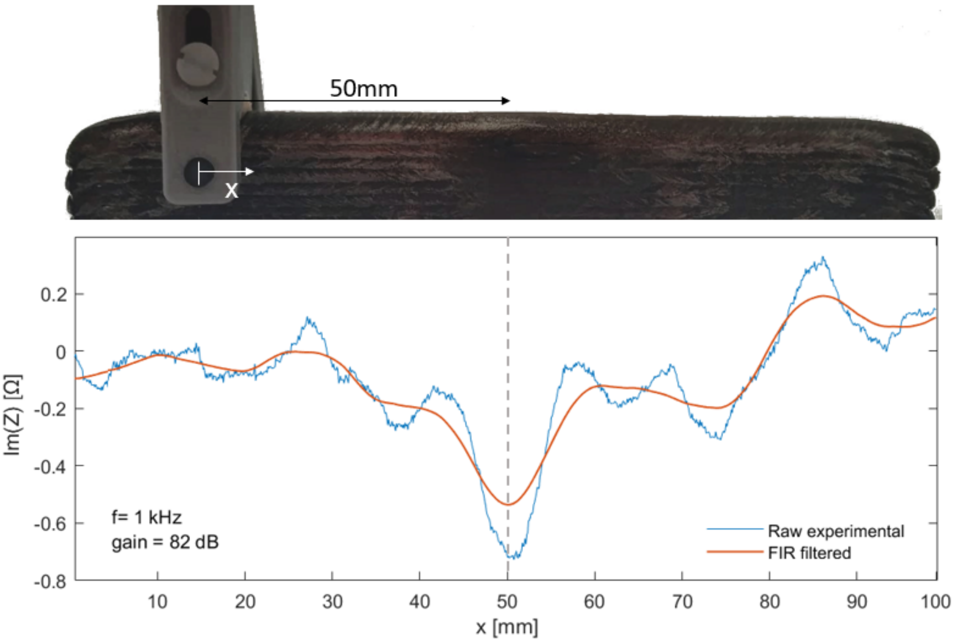

Figure 4.11: ECT results for an internal defect 350 µm thickness and 5 mm in length.

There is an important aspect to consider when comparing this probe to its IOnic predecessor: the placement of the excitation coils on the sides of the sample means that the probe can only start the inspection when at least 2 or 3 layers have been deposited i.e the WAAM wall has to reach a certain height so that the SEP's excitation coils reach the sample. However, this might be easily overcome by using a complementary inspection method on the first layers, such as placing an UT probe on the bottom of the base plate.

In conclusion, the main goal of this chapter was accomplished. The IOnic probes previously developed proved to achieve promising results in ferromagnetic materials and the new SEP probe design showed improvements in the detection capabilities of internal defects. In short, ECT proved to be a promising solution for the in-line inspection of WAAM steel parts, although further research is needed in order to overcome challenges related to the morphology of the defects and materials to inspect.

Chapter 5

UT inspection

As stated on the literature review, ultrasonic testing was indicated, according to Lopez et al. [1], as being one of the most promising techniques for the in-line inspection of WAAM parts. In a more recent study, Lopez et al. [4] studied the applicability of phased array ultrasonic testing (PAUT) in the inspection of WAAM produced walls. PAUT systems utilise multi-element probes, which are individually excited. By exciting each element in a controlled manner, a focused beam can be generated and steered by the use of proper software. Two and three dimensional views can be generated showing the sizes and locations of any flaws detected. This chapter aims to study two aspects of the UT inspection of WAAM produced parts in order to improve its capabilities: surface texture and coupling medium.

Regarding surface texture, the main focus of the last mentioned reference was to evaluate the influence of surface roughness in the ultrasonic signal response. However, the impact of roughness alone is not enough to characterize the UT behaviour. As an example, one of the solutions presented for this problem is machining the top surface of the WAAM wall, but it is known that roughness after machining is related to the tool geometry, cutting parameters and relative motion between the cuting tool and the workpiece on the surface finish profile [56]. This means that machining the surface does not guarantee less roughness that the original sample (although highly likely) and what's actually being directly improved is the other constituent of surface texture: waviness. Most articles where this association between UT and roughness is made are related to processes where roughness is the main challenge for surface finish, such as die castings for example. In the case of WAAM, waviness is the predominant issue.

For this reason, the present chapter was firstly focused on developing a realistic PAUT inspection model on the commercial simulation and analysis software CIVA in order to understand the influence of waviness in inspection. An experimental validation was also performed to verify the simulation's results. On a second approach, the potential of using solder paste as UT couplant for the high temperature inspection of WAAM parts was analysed. This motivation will be further explained later on the respective chapter 5.3.

5.1 Numerical inspection of defects

CIVA^{TM} is a simulation and analysis commercial software specifically developed for NDT applications, whence why it was used in this work. This software permits the control of a wide range of options from types of probes to different defect scattering models, allowing the prediction of various inspection techniques.

CIVA's theoretical model for beam computation is based on a geometric model of pencil propagation. The purpose of the pencil model is to predict the various elostodynamic quantities corresponding to bulk waves radiated from a source point to a computational point, over ultrasonic energy paths. Computation usually takes place in two stages. In stage one, the different energy paths are determined according to Snell-Descartes laws (generalized to anisotropc media). In stage two, the vectorial nature of the elastodynamic fields is credited by determining the polarization directions of the various waves according to Christoffel's Laws.

Regarding roughness, this parameter is statistically defined by the mean square R_q of height variation along the rough profile considered, but one can also define it by simply considering the mean value of the same function. This is denoted by R_a and its value was kept at 75 µm throughout all of the simulations as it's influence on the UT beam was already studied [4]. For now, it is important to note that, in CIVA, when the coefficient Ra is to be entered, the transmission coefficient for L or T waves is modified by a factor that is a function of the angular frequency, ω. Similarly, the reflection coefficient is also affected.

As for waviness, instead of approximating it to the value of R_a while assuming that the surface of the part is planar, different CAD models similar to WAAM walls were designed, as it is not possible to directly introduce texture/waviness in this particular software. That being said, the influence of the transducers' characteristics on ultrasonic signals for wavy surfaces was investigated. Similarly to Lopez et al. [4], frequency and active aperture were selected as the parameters that influence the inspection of irregular surfaces.

In order to introduce waviness into CIVA, several CAD models were experimented. With the objective of designing the most realistic model possible, the data gathered from the perfilometer analysis of chapter 3.4.1 was imported to Solidworks which created splines through the discrete points. This attempt was not successful as the data resolution was to high for CIVA to process. For a realistic inspection the mesh would have to be extremely refined leading to a unacceptably long computation time. For this reason, a simplified approach was used. From the study of chapter 3.4.1, the maximum waviness was around 0.04 mm with the use of an oscillation deposition strategy. Therefore, a CAD surface was designed keeping that maximum value for 10 mm steps in the X direction, as illustrated in figure 5.1.

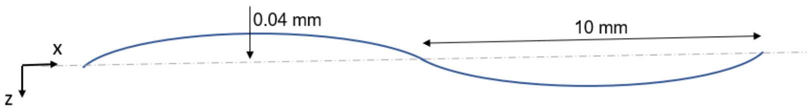

Figure 5.1: Wavy surface CAD geometry.

Then, a parallelepiped CAD specimen was created with two halves having different surfaces: one planar and the other wavy, as seen in figure 5.2. Because of CIVA's comparative scale, having two different surfaces in the same specimen instead of two models permitted a direct comparison of the results in the inspection simulation.

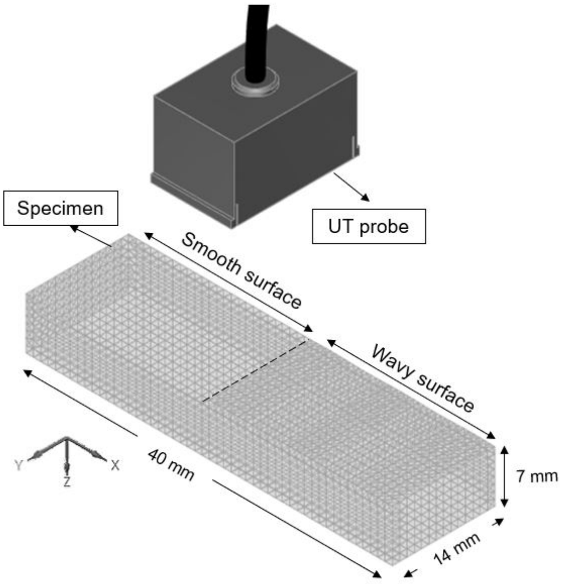

Figure 5.2: Final inspection model.

The material chosen for the specimen was isotropic carbon steel with density ρ, of 7.8 $\mathrm{g\,cm^{-3}}$ and longitudinal wave velocity of 5900 $\mathrm{m\,s^{-1}}$. Roughness R_a was kept at 75 µm, as previously mentioned.

The mesh was refined with accuracy of 0.001 mm which is the maximum discrepancy between the surface of the specimen defined by the CAD file and the surface meshed into triangles. The minimum element size was 0.001 mm as well. This refinement was sufficient to obtain reliable results while keeping an acceptable computation time.

An immersion type probe with linear phased array pattern and 32 elements with flat focusing was selected. The chosen frequency was 5 MHz. Due to the fact that the average layer height in WAAM is around 2.5 mm, single point focusing in the inspection plane was selected along the longitudinal axis, Z = 2.5 mm, as this was the region of interest. The uniform delay laws were calculated for longitudinal waves accounting for backwall reflection and finally, a water path of 20 mm between the specimen and the UT probe was used, with ρ = 1 $\mathrm{g\,cm^{-3}}$ and primary wave velocity of 1483 $\mathrm{m\,s^{-1}}$. The attenuation laws were neglected both in the specimen and water medium, to simplify the analysis.

5.1.1 Beam computation modelling

Having set most computation parameters, the probe active aperture was studied in order to optimize the number of elements needed for inspection, as presented in figure 5.3. Due to the comparative nature of CIVA's colour scale, these three images cannot be compared directly i.e the maximum acoustic pressure (light blue area) has a different dB value for each simulation.

For 10 active elements or less, the acoustic pressure reaches its maximum value on the top surface, which is not ideal as this promotes higher amplitudes on the first (surface) echo camouflaging the defects

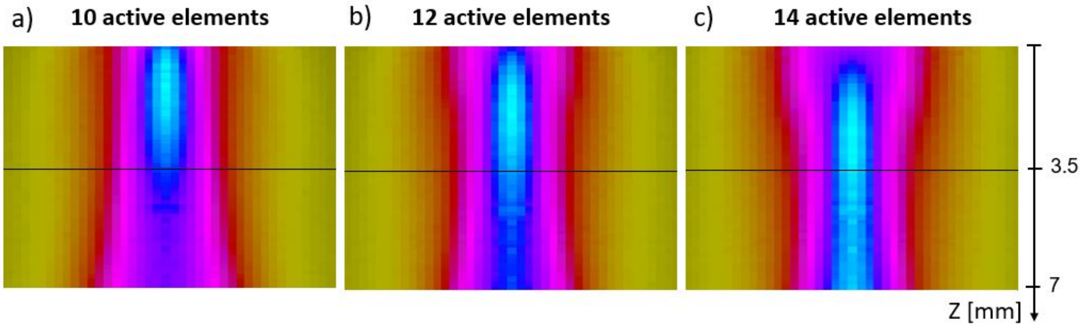

Figure 5.3: Visualization of the beam spread for different apertures, using a 5 MHz probe.

to be detected. In contrast, with 14 active elements there is no significant acoustic pressure on the top of the sample's surface and the light blue area is spread through the sample's height which can lead to noisesome results. Therefore, 12 elements were selected as the maximum pressure is focused on the region of interest and shortly distanced from the top surface.

Secondly two simulations were carried out placing the probe over the different surfaces. The results of this beam computations are shown in figure 5.4.

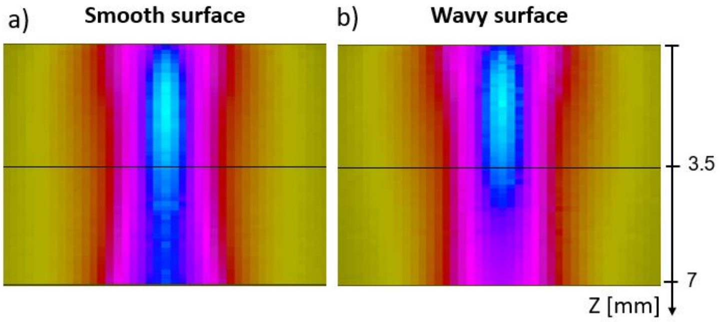

Figure 5.4: Visualization of the beam spread for different surface textures.

The main difference between these two computations can be seen on the 3.5 to 7 mm mark. One can clearly see a significant decrease in acoustic pressure (dark blue area) on the wavy surface example, which can compromise the probe's ability to detect deeper defects. This test reaffirms that micrometric waviness variations in a WAAM sample induce significant changes to the ultrasonic beam.

5.1.2 Inspection simulation

After evaluating the impact of surface waviness in the UT beam spread, a defect inspection simulation was performed by placing two 3 mm diameter flat bottom hole defects, 2.5 mm under the surface, as can be observed in figure 5.5. Flat bottom holes are a type of reflector commonly used in reference standards where the end (bottom) surface of the hole is the reflector. Defect A is placed under the smooth surface where roughness is the only surface condition, and defect B under a more realistic surface that complies both roughness and waviness as previously discussed. One can also see the scanning path trajectory which was done in 2 mm steps to minimize computation time, following the x direction.

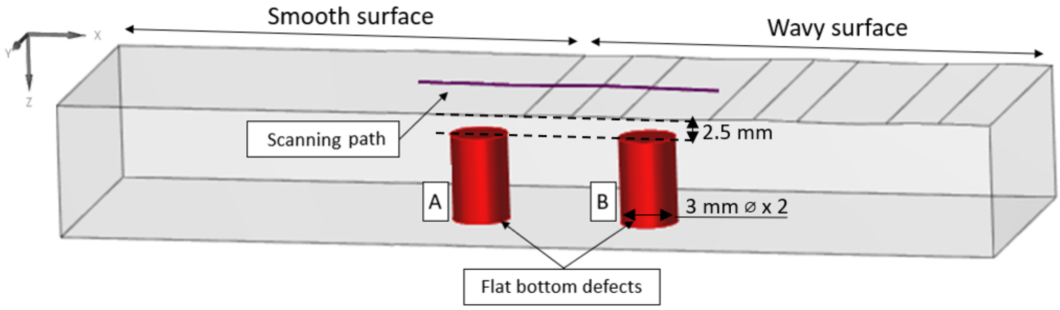

Figure 5.5: UT inspection model used with two 3 mm diameter flat bottom holes, 2.5 mm under the top surface.

The results of this inspection are shown in figure 5.6 C-scan view is presented for a more visual insight oh the phenomena.

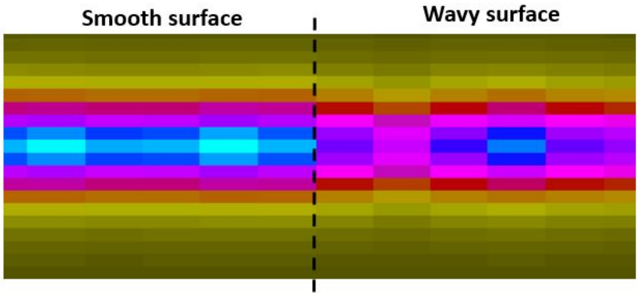

Figure 5.6: C-scan view of the interface between two different surfaces.

This view shows the interface between the two different top surfaces. One can clearly see that, on the wavy side, the acoustic pressure distribution is more diffused and there is a decrease in the maximum value (light blue area) compared to the smooth counterpart.

in figure 5.7, the two defects are shown in their B-scan view. These examples were took by placing the inspection window only over the defects in order to neglect the surface echo to facilitate the comparison between flaws. This can be done directly, in contrast to the beam computation, because these examples were took from the same inspection simulation.

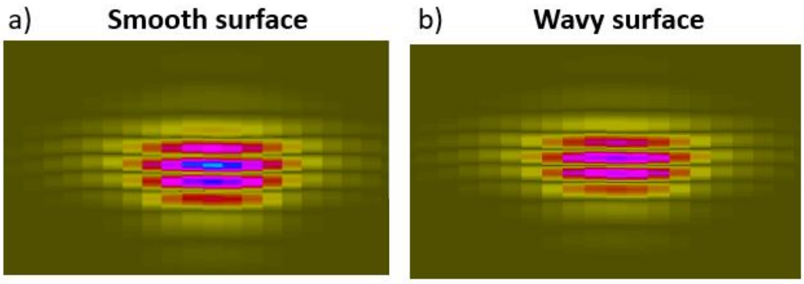

Figure 5.7: B-scan view of two flat bottom hole defects under different surfaces.

One can clearly see that both defects present themselves with similar acoustic pressure distributions, although there's a slight decrease in the wavy surface example. If this drop is significant enough depending on the degree of waviness, the defect detection might be concealed.

Finally, 5.8 a) shows the A-scan for the two different surfaces. As was predictable from the previous C-scan, one can clearly see a drop of about 35% in amplitude of the first echo. Figure b) shows the defect echo detailed, neglecting the surface, where the amplitude drops approximately 20%. Although the beam was optimized to detect a defect in the region of interest, one can observe that for a flat bottom hole 2.5 mm under the surface, inspection might be compromised as the defect gets overpowered by the entry echo.

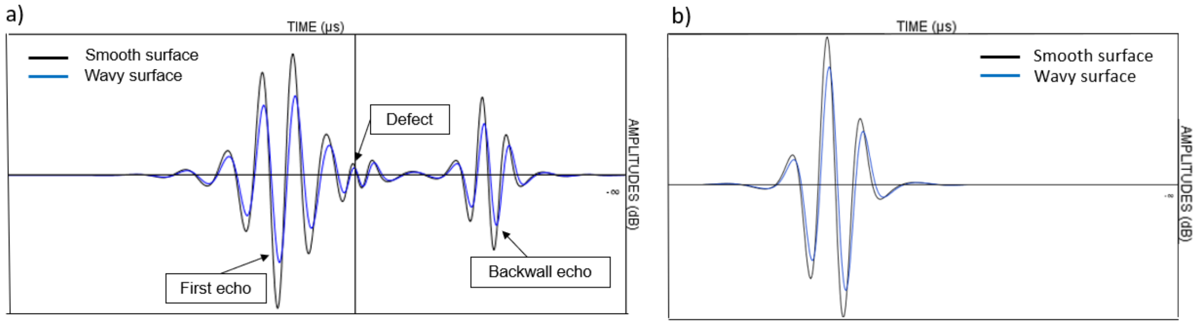

Figure 5.8: A-scan results for the smooth and wavy surfaces.

In conclusion, the developed model presents a realistic method to understand the effect of surface texture in the inspection of WAAM parts. This enables a better selection of probes, apertures and other inspection parameters, allowing to predict how the sound pressure enters the part. However, this analysis can only be qualitative as the maximum energy that is seen for different apertures may be significantly distinct. For this reason, the following experimental validation of the model is followed.

5.2 Experimental validation

With the objective of reproducing the previous simulation model, 3 mm diameter flat bottom holes were drilled 2.5 mm under the surface in a WAAM steel sample with similar dimensions to the previous model. The samples used were analysed with a surface perfilometer and had a maximum waviness of around 0.02 mm using the same deposition and welding parameters. Firstly, a conventional Olympus small-footprint probe with 5 MHz of frequency was used both with a planar and curved wedge using UT couplant gel. The unsatisfactory results show that the inspected material of the WAAM sample has a bigger influence than expected. From LASIMM's internal reports it is known that the same probe detected similar defects at the same depth on aluminium samples.

Because of the unsatisfactory results using the previous probe, the followed experiments were made in immersion (water coupling) with two PAUT probes: an IMASONIC 3.25 MHz with 20 elements plus mechanical focus, and an OLYMPUS 5 MHz with 32 elements. The last was identical to the probe used on CIVA's simulations. Both probes can be seen in figure 5.9.

For the first probe, no defect was detected despite the number of active elements or water column height used. With the 5 MHz probe, using 1 active element a very muted defect could be seen, but its echo would be almost completely overwhelmed by the surface echo, as predicted by the inspection

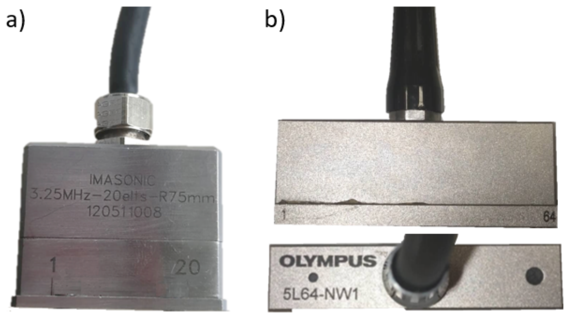

Figure 5.9: Phased array UT probes used: a) IMASONIC 3.25 MHz 20 elements, b) OlYMPUS 5 MHz 32 elements.

simulations on CIVA. For this reason, a different approach was taken. Half of a WAAM wall's top was machined seeking to remove as less material as possible while the other half kept its original texture. Two pairs of 3 mm flat bottom holes were placed 4F mm under surface and radiography tests were done to verify the measurements and positioning of the defects, as can be seen in figure 5.10 a).

Both probes detected all four defects more or less clearly, but the best results were encountered with the OLYMPUS 5 Mhz with only one active element. Figure 5.10 b) shows the C-scan of this inspection.

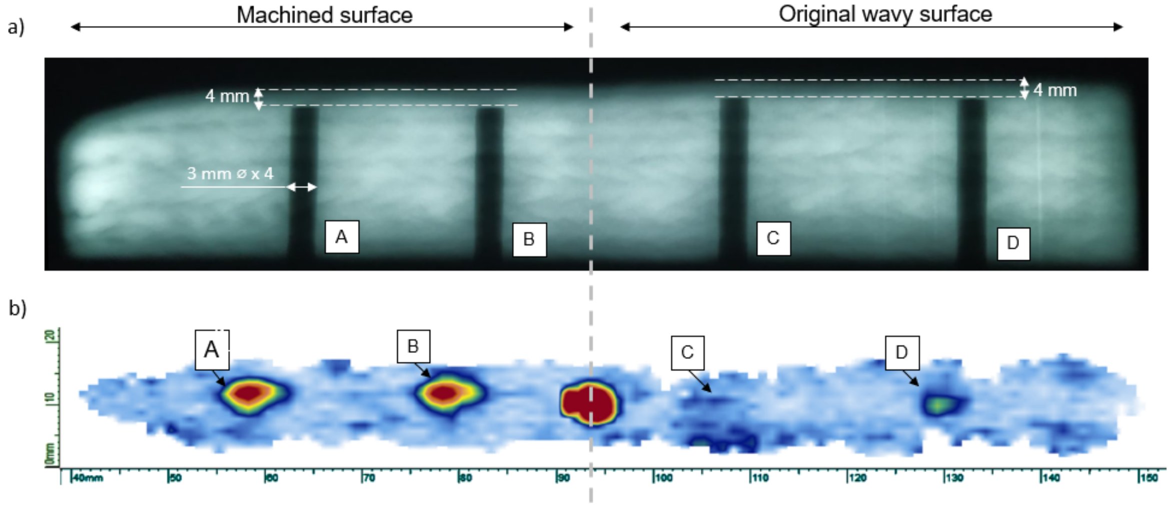

Figure 5.10: a) Radiography results; b) C-scan view for OLYMPUS 5 MHz probe.

The last figure shows that defects A and B on the machined half are clearly detected and exhibit very similar acoustic pressure distributions. On the other hand, defects C and D on the original wavy side appear more muted. Moreover, defect D is more easily detectable than C. This shows that for the inspection of WAAM parts, the defect detectability is highly dependent on the local waviness that the probe encounters.

Defects A and D were selected to be compared and their B-scan and A-scan results can be seen in figures 5.11 and 5.12 respectively.

By observing figure 5.11 a) one can see the defect clearly detected on the B-scan with maximum acoustic pressure. From figure 5.11 b), the difference between the peaks of the first echo and the defect was measured indicating a distance of 4.2 mm which is proximate to the real depth of the defect.

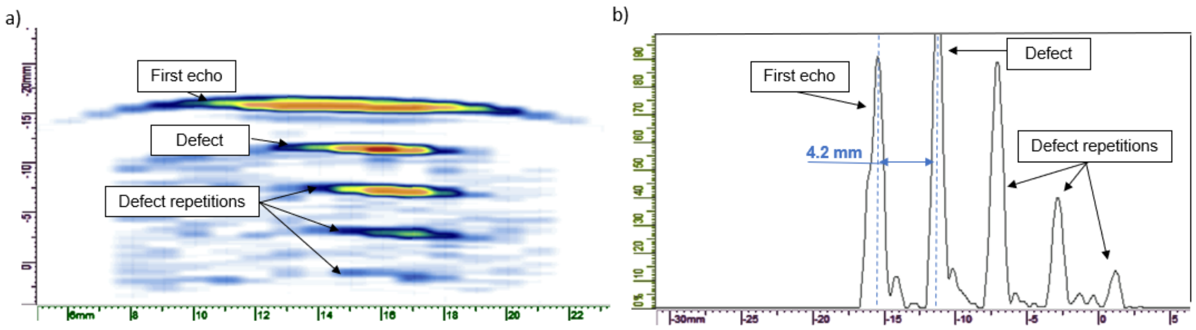

Figure 5.11: Defect A under machined surface, inspected with a 5 MHz PAUT probe: a) B-scan b) A-scan.

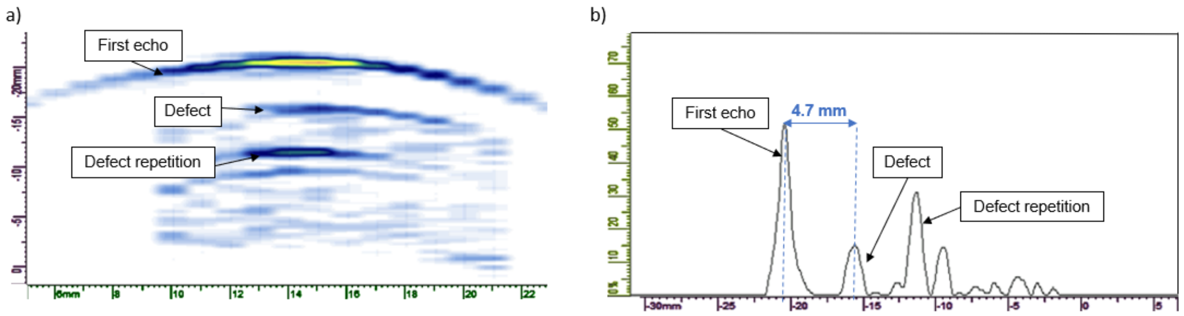

Figure 5.12: Defect D under WAAM surface, inspected with a 5 MHz PAUT probe: a) B-scan; b) A-scan.

Although an effort was made to remove as less material as possible while machining, this process also flattened the surface eliminating the characteristic curvature of the samples which might have also contributed for the successful result of this inspection.

For defect D under the original WAAM wavy surface, shown in figure 5.12), it was still detected although a general decrease in amplitude is evident compared to the defect on the machined side, as was predicted on the previous simulations. Here, the surface curvature is evident on the first echo. On the A-scan, the distance between the defect and the surface was overreached by almost 1 mm. Comparing both defects A and D, the defect echo amplitude decreased around 80% on the wavy side which is a very significant drop. The effect of surface waviness becomes even more evident by observing the D-scan view in figure 5.13.

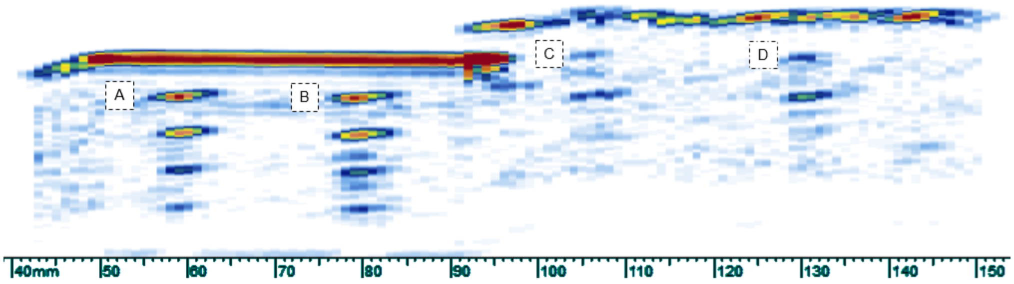

Figure 5.13: D-scan view of WAAM samples showing all four flat bottom defects.

While every defect was able to be detected more or less clearly depending on its localization, there are some considerations to be done relatively to dimensioning said defects. This is crucial for in-line inspection as flaws need to reach a critical size in order to be removed by the subtractive module of the LASIMM hybrid machine.

For defects A and B under the machined half, both could be dimensioned using the same 6 dB rule that is a commonly understood practice for length sizing discontinuities in welds. This technique defines the defect length as half (6dB) of the maximum amplitude obtained while the transducer is scanned over the flaw. Both holes were measured at 2.9 mm using this rule, which is acceptable as it is only 0.1 mm away from the real diameter. On the other hand, defect D wasn't able to be correctly dimensioned with the past method, needing a more constricted rule of 3 dB. Defect C was not possible to be dimensioned accurately at all, with any of the mentioned rules, which means that the capabilities of correctly sizing a defect on a typical WAAM surface might be compromised depending on what local waviness the probe encounters.

Comparing to the previous simulation models, they served the purpose of understanding sound behaviour in WAAM parts with and without surface machining. However, in practice, 1 active element presented the best results for defect inspection instead of the 12 active elements predicted by the simulations. This is due to the fact that quantitatively, the sound energy was too high for over one active element producing an entry echo that camouflaged the defects during the experiments. This was not predicted in the qualitative analysis performed on CIVA. Other differences between the simulations and experiments can also be explained due to the simplifications made by neglecting the attenuation phenomena and by simplifying the part geometry.

In conclusion, PAUT proved to be a reliable method for inspecting WAAM steel samples although sizing can be difficult depending on the surface conditions. However, to improve inspection, machining the sample's top might be favorable when applicable.

5.3 Solder paste

Couplants are essential for providing the necessary link between transducers and materials in ultrasonic testing as it enables sound waves generated by the transducer to be efficiently transmitted into a material. It is generally necessary because the acoustic impedance mismatch between air and solids (i.e. such as the test specimen) is large. Therefore, nearly all of the energy is reflected and very little is transmitted into the test material. The couplant displaces the air and makes it possible to get more sound energy into the test specimen so that a usable ultrasonic signal can be obtained. In contact ultrasonic testing a thin film of oil, glycerin or water is generally used between the transducer and the test surface.

When regarding the in-line inspection of WAAM steel parts, there are some challenges in coupling that need to be overcome mostly related to the high temperatures involved in the process. If water is used, it will vaporize instantly at 100$^\circ C$ which will difficult the chance of active coupling. This problem is even more evident in steel, as temperature cycles can range between 300-1150 $^\circ$C or higher depending on the heat input [2]. One of the solutions is to increase the cooling time between layers, but that would also increase the lead time of manufacturing which is one of the biggest advantages in WAAM.

In alternative to water, high temperature UT Couplants are usually used in welds, but these tend to leave residues between layers which makes them unsuitable for in-line inspection [LASIMM internal report]. Therefore, the possibility of using solder paste as UT coupling was tested. The premise was this paste would be suitable for in-line inspection of WAAM parts as it formulated to withstand higher temperatures. Moreover, because it is water based, the UT signal should not be compromised.

Therefore, this chapter serve two purposes. Firstly, to understand if the use of this solder past will have any detrimental effect to the microstructure and structural integrity of WAAM parts. Secondly, to verify experimentaly is said couplant can be used for UT inspection. The conducted tests were done for two samples manufactured with the same parameters: WFS = 7 m/min, WFS/TS = 40 and 4 minutes of cooling time. The control sample with no solder paste was designated as P1. For sample P2, the solder paste was applied to every layer 1 to 2 minutes after the bead was deposited as to allow some time for cooling to avoid instant vaporization of the liquid. This information is summarized on table 5.1.

Table 5.1: Samples production strategy.

Sample	Couplant between layers
P1	×
P2	✓

5.3.1 Microstructure analysis

For this analysis, the same procedure as chapter 3.4.2 was performed. Firstly, a traversal section of the samples was removed, resin-wrapped and polished. Finally, 2% Nital was used as contrast. The results from a equivalent central portion of both samples are presented in figure 5.14.

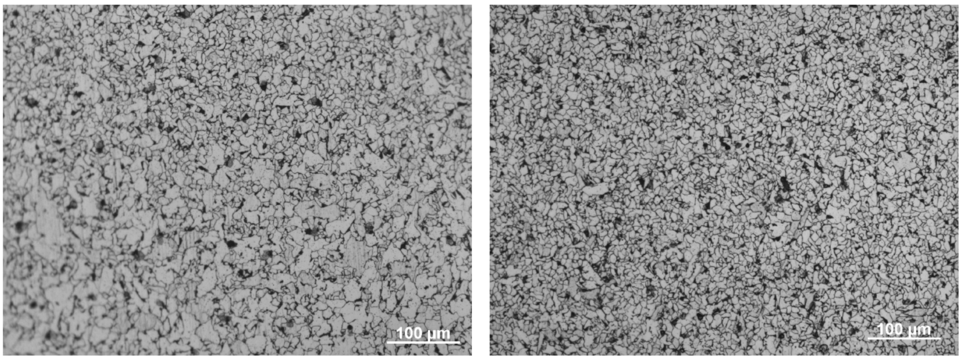

(a) P1

(b) P2

Figure 5.14: Grain size variation with and without solder paste application.

As can be seen, at the microstructural level, the main difference observed when comparing the two samples is the grain size. On the sample with solder paste between layers (P2), the grain size is smaller on average and more uniform comparing to sample P1. This could be explained by the fact that some of the heat is transferred to the liquid when the paste is being applied meaning that the welding bead will tend to cool more rapidly. The results are consistent with the theory that rapid cooling is associated to smaller grain formation.

Besides grain size variations, neither sample P1 or P2 presented visible defects and similar micro-constituents were observed through both samples in equivalent regions. This serves to show that the use of the solder paste does not significantly influence the deposited material at a microstructural level.

5.3.2 Mechanical behaviour

The mechanical properties of the samples with and without application of the solder paste were studied as they relate to the performance of the material. Therefore, tensile and hardness tests were conducted.

Typically, AM produced parts have an oriented grain structure, which means that the mechanical properties can differ in direction. For this reason, the tensile test specimens were removed from the WAAM walls accordingly to the orientation of the build as ilustrated in figure 5.15. The specimens were fabricated following the ISO 6892-1-2009 standard.

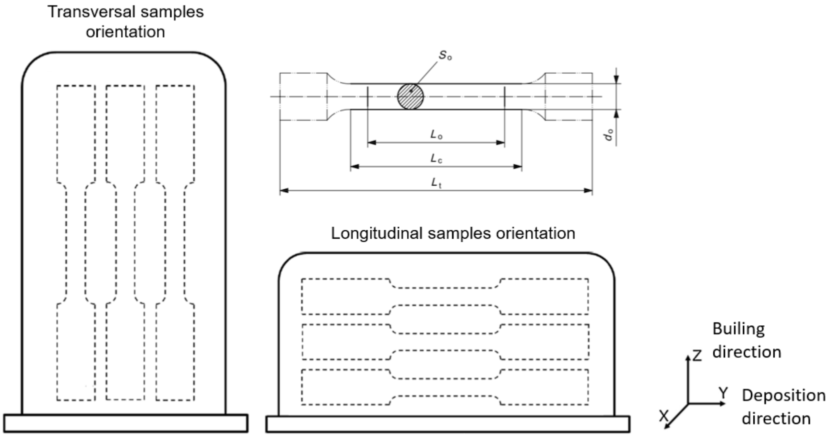

Figure 5.15: Scheme of the tensile test specimens extracted from WAAM samples according to ISO 6892-1-2009 standard.

The uniaxial tensile tests were performed in a Instron 4507 electromechanically actuated static load frame machine, with a maximum load capacity of 200 kN. Specimens were tested at room temperature using an extensometer to measure changes in the length. The stress-strain curves are shown in figure 5.16 a) for a more visual examination for 2 pairs of selected specimens. Figure 5.16 b) shows the statistical representation of all tested specimens, where the sample standard deviation (s), of the error bars was calculated using equation 5.1:

$$s = \sqrt{\frac{\sum_{i=1}^{n} (x_i - \overline{x})^2}{n-1}} \tag{5.1}$$

Where x_i is each data value, $\overline{x}$ is the mean of x_i, and n the number of data points.

in figure 5.16 a) the selected stress-strain curves are representative of a typical mild-steel curve with discontinuous yielding (the material reaches an upper yield point before dropping rapidly to a lower yield point) and ductile behaviour. Some differences can be seen for the transversal (y) and longitudinal (z) components which may be related to preferential orientation of austenite grains during solidification. Nevertheless most values fall on the catalogued range of UTS = [500,640] MPa a for 80% Ar + 20%

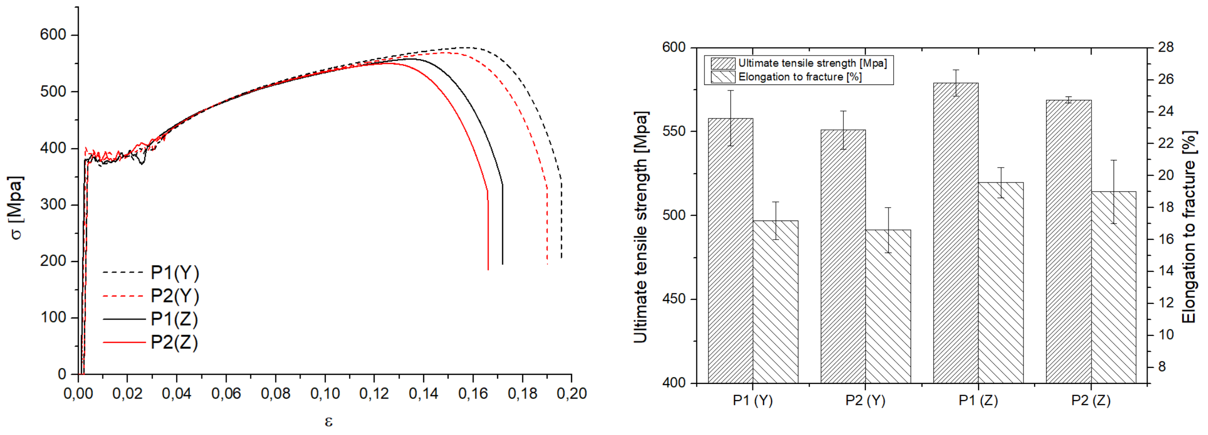

(a) Stress–strain curve.

(b) Ultimate tensile strength (UTS) and elongation to fracture of the tested samples.

Figure 5.16: Tensile test results.

CO2 according to the wire manufacturer data sheet [57]. Although the same reference indicates a ϵ_{min} of 20%, the differences can be explained by dissimilarities in the welding process, shielding gas and experimental conditions.

However, the main interest of this study was not to evaluate the mechanical proprieties of the manufactured walls, but to compare the samples with and without solder paste application. Figure 5.16 b) suggests that this differences in UTS and elongation to fracture between samples P1 and P2 are not statistical significant as the results are very similar. The greater values of standard deviation can be justified by the fact that the samples were cut from different areas of the built WAAM walls. Ultimately, one can infer that the solder paste usage does not adversely affect the mechanical proprieties of the deposited material in a significant manner.

Finally, hardness tests were done by calculating the Vickers Hardenss (VH) along the building direction of the samples using a Duramin Struers machine. The results are presented in figure 5.17.

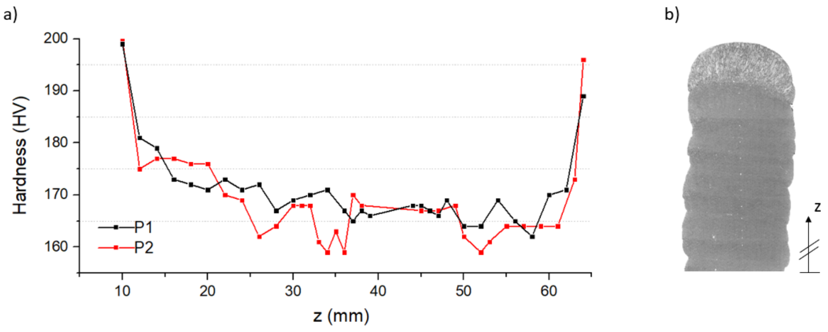

Figure 5.17: Hardness test results and marked indentations.

Both samples P1 and P2 presented similar behaviour. Although small deviations can be observed, the differences between the peak values are not significant, allowing to conclude that the mechanical properties are homogeneous over each layer, despite variations of the involved temperatures. This was true except for the initial and last layers where the hardness was comparatively higher. The fast cooling rate in the first deposited layers, aided by the cold substrate and its capacity for heat dissipation, justify the higher hardness observed in this region. In the top layers, the microstructure is different and easily distinguishable in figure 5.17 b), similar to a single pass weld were acicular ferrite and grain boundary ferrite formation is promoted. This exhibits a predominantly columnar grain structure with relatively higher hardness values.

In brief, the tensile and harness tests revealed similar mechanical behaviour between the samples with and without solder paste, which is a good indicative that its application as couplant will not injure the parts' performance.

5.3.3 Elemental composition

Last but not least, scanning electron microscopy (SEM) was conducted in order to verify if the solder paste application had any influence on the chemical composition of the steel samples. This technology works by scanning a focused electron beam over a surface to create an image. The electrons in the beam interact with the sample, producing various signals that can be used to obtain information about the surface topography and composition. The selected areas of examination on the samples are shown in figure 5.18 were the the differences in grain size can be observed once again.

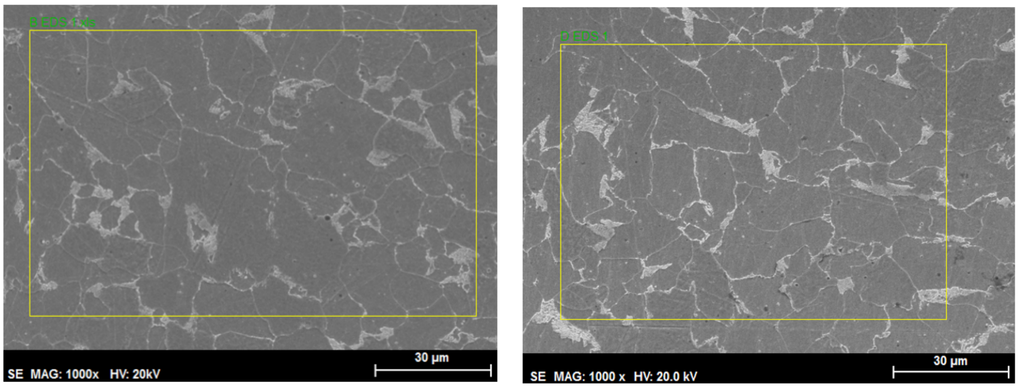

(a) Sample P1

(b) Sample P2

Figure 5.18: Selected areas of SEM analysis.

The elemental composition of microscopic particles or regions on a sample's surface is analysed using a energy dispersive x-ray spectrometer (EDS) attached to the SEM. EDS micro analysis is performed by measuring the energy and intensity of the signals generated by the focused electron beam scanned across the specimen. EDS is most often used for qualitative elemental analysis to determine which elements are present, and to conclude their relative abundance.

The results in figure 5.19 show that both samples P1 and P2 had identical chemical composition as the same number of elements were present (C, Mn, Fe, Si) and in approximately the same quantities. This means that the application of the solder paste did not alter the sample's elemental composition.

5.3.4 Experimental validation

After concluding that the use of the solder paste would not be detrimental to the WAAM manufactured parts, it was necessary to experimentally validate if this would be a viable couplant for UT.

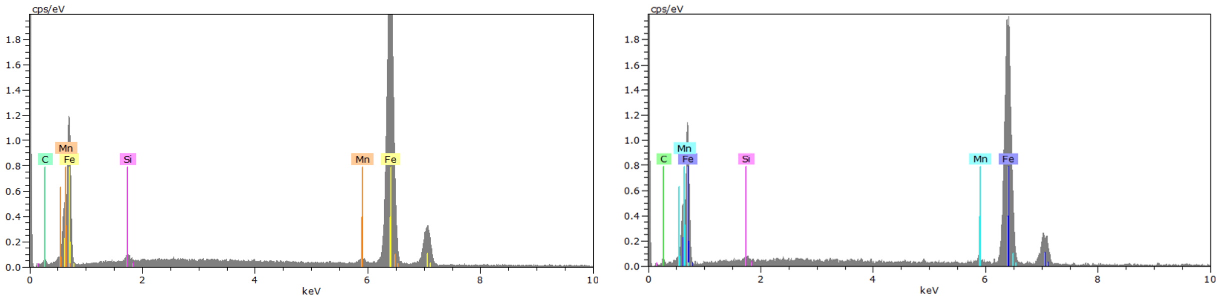

(a) P1.

(b) P2.

Figure 5.19: Elemental composition of the samples.

To do so, a conventional 5 MHz UT probe was used on the machined half of the previous UT experiments from chapter 5.2 to inspect the same 3 mm flat bottom hole, 4 mm under surface. The results can be seen of figure 5.20.

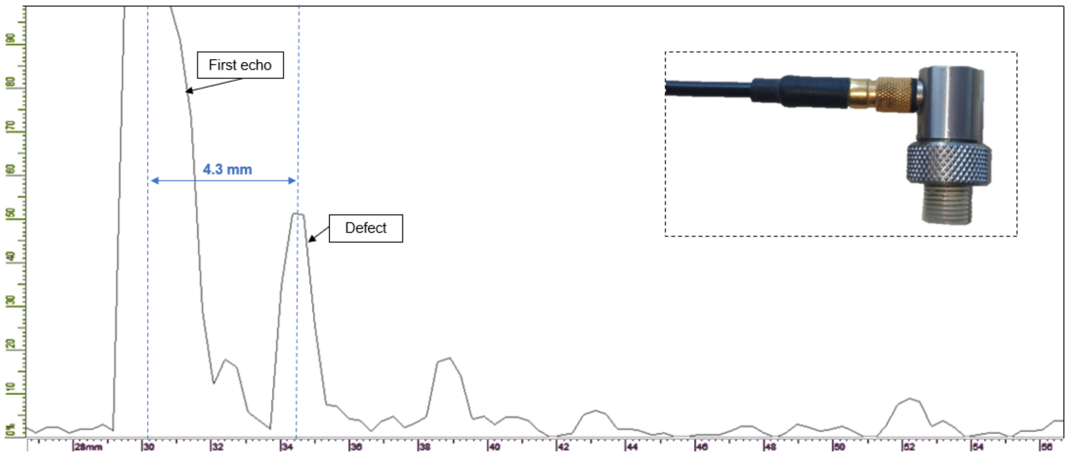

Figure 5.20: A-scan results for 5 MHz conventional UT probe using solder paste as couplant.

As one can see, the probe clearly defects the defect with a satisfying SNR, proving that the solder paste can be used as an UT coupling similar to water, without compromising results.

In conclusion, the use of solder paste in ultrasonic coupling shows promising results for the inspection of WAAM steel parts when compared to water or high-temperature couplants as the UT signal was satisfactory and no substantial differences in mechanical behaviour or chemical composition between samples were encountered.

Chapter 6

Conclusions and future work

6.1 Conclusions

The broad goal of this thesis was to contribute for the LASIMM project and the evaluation of parts produced by WAAM using non-destructive techniques. More specifically, there were two main objectives be accomplished as explained in the introduction and the collected conclusions are the following.

Regarding the first objective of process optimization for surface texture minimization:

- The use of triangular weaving as the deposition strategy was able to significantly decrease the waviness profile down to under 0.01 mm from the oscillation counterpart with 0.045 mm. This indicates a reduction of about 78% in waviness.

Concerning the consolidating EC and UT techniques for the detection of internal flaws in steel WAAM parts:

- The new SEP EC probe design showed improvements over the previous IOnic customized models regarding defect detectability. This probe was able to detect a 350 µm x 5 mm internal defect in a carbon steel WAAM sample with acceptable SNR;
- UT inspection showed best results for an OLYMPUS 5 MHz phased array probe. Fat bottom hole defects of 3 mm diameter, 4 mm under surface were detected in a WAAM sample with its original waviness profile;
- Results with a conventional small-footprint 5 MHz OLYMPUS probe show that inspection in WAAM steel samples was unsuccessful in contrast to the same tests performed on aluminium [LASIMM -internal report]. This means that, in the case of steel, phased array should be used when there is no machining between layers;
- The use of solder paste as high temperature UT couplant is promising as it did not adversely interfered with the steel's mechanical proprieties and chemical composition. Experimental results were also successful.

As with most things, an all-purpose solution for the inspection of WAAM parts can't be achieved, as each technique has its own advantages and limitations. For example, in the WAAM steel part shown in the introduction (figure 1.1), UT would be most adequate at the bead intersections than ECT. During the first layers, using UT under the base plate would be helpful as the SEP probe needs a certain height to start inspection due to the lateral excitation format. However, ECT is more adequate for smaller widths compared to the tested phased array probes and doesn't have de ”dead layer effect” problem that UT has in inspecting the first layers. This means that the most adequate inspection should be a combination of both ECT and UT techniques. For a company that decides to invest in a in-line inspection equipment, a thorough investigation on the part's material, geometrical complexity, and type of defects to inspect must be done *a priori* in order to understand what technique is the most advantageous if not both.

6.2 Future Work

There are still many future work directions this research can take. Considering the preliminary results, the following studies could be followed.

Regarding deposition:

- In this thesis, triangular weaving was compared to oscillation, but many different strategies are available using the fronius CMT equipment combined with the KUKA robot, such as trapezoidal, spiral and figure-of-eight weaving that might also show improvements in surface quality.

Concerning EC inspection:

- The effect of temperature must be taken in consideration while using the SEP design, as the high temperatures involved in the WAAM process may damage the probe causing undesired impedance variations that may hinder the inspection. For this reason, a study on the lift-off should be performed in order to evaluate the maximum distance the SEP probe can be from the sample's surface. Moreover, some test at high temperatures should be performed as it is possible that longer cooling times have to be used, compromising the lead time of manufacturing which was one of the main advantages of WAAM due to its higher deposition rates.

- Although the results obtained in steel presented an acceptable SNR, it should be worthwhile to evaluate if saturating the material would benefit the signal, as this is a common solution for EC testing in ferromagnetic materials.

Finally, about UT inspection:

- More realistic and smaller internal defects should be tested, as a bigger challenge relatively to flat bottom holes.

- High temperature tests using the solder paste should be conducted in order check for the couplant vaporization temperature and to evaluate the cooling time needed between layers that doesn't compromise lead time.

Bibliography

[1] A. Lopez, R. Bacelar, I. Pires, T. G. Santos, J. P. Sousa, and L. Quintino. Non-destructive testing application of radiography and ultrasound for wire and arc additive manufacturing. *Additive Manufacturing*, 21:298–306, 2018.

[2] T. A. Rodrigues, V. Duarte, R. M. Miranda, T. G. Santos, and J. P. Oliveira. Current Status and Perspectives on Wire and Arc Additive Manufacturing (WAAM). *Materials*, 12:1121, 2019.

[3] B. Wu, Z. Pan, D. Ding, D. Cuiuri, H. Li, J. Xu, and J. Norrish. A review of the wire arc additive manufacturing of metals: properties, defects and quality improvement. *Journal of Manufacturing Processes*, 35:127–139, 2018.

[4] A. Lopez, J. Santos, J. P. Sousa, T. G. Santos, and L. Quintino. Phased Array Ultrasonic Inspection of Metal Additive Manufacturing Parts. *Journal of Nondestructive Evaluation*, 38:62, 2019.

[5] J. B. Bento, A. Lopez, I. Pires, L. Quintino, and T. G. Santos. Non-Destructive Testing for Wire + Arc Additive Manufacturing of aluminium parts. *Additive Manufacturing*, 27:440–450, 2019.

[6] M. Attaran. The rise of 3-D printing: The advantages of additive manufacturing over traditional manufacturing. *Business Horizons*, 60:677–688, 2017.

[7] F. Caviggioli and E. Ughetto. A bibliometric analysis of the research dealing with the impact of additive manufacturing on industry, business and society. *International Journal of Production Economics*, 208:254–268, 2019.

[8] L. A. Verhoef, B. W. Budde, C. Chockalingam, B. García Nodar, and A. J. van Wijk. The effect of additive manufacturing on global energy demand: An assessment using a bottom-up approach. *Energy Policy*, 112:349–360, 2018.

[9] L. Gasman. *Additive aerospace considered as a business.* Elsevier, 2019.

[10] C. Culmone, G. Smit, and P. Breedveld. Additive Manufacturing of Medical Instruments: A State-of-the-Art Review. *Additive Manufacturing*, 27:461–473, 2019.

[11] W. E. Frazier. Metal additive manufacturing: A review. *Journal of Materials Engineering and Performance*, 23:1917–1928, 2014.

[12] F. Martina. *Investigation of methods to manipulate geometry, microstructure and mechanical properties in titanium large scale Wire+Arc Additive Manufacturing*. PhD thesis, 2014.

[13] J. Bento. *Non-Destructive Testing of large metal parts produced by Wire Arc Additive Manufacturing Development of customized Eddy Currents probes for the online Non-Destructive Testing of aluminium Wire Arc Additive Manufactured parts*. PhD thesis, 2018.

[14] W. J. Sames, F. A. List, S. Pannala, R. R. Dehoff, and S. S. Babu. The metallurgy and processing science of metal additive manufacturing. *International Materials Reviews*, 61:315–360, 2016.

[15] P. K. Gokuldoss, S. Kolla, and J. Eckert. Additive manufacturing processes: Selective laser melting, electron beam melting and binder jetting-selection guidelines. *Materials*, 10(6), 2017. ISSN 19961944. doi: 10.3390/ma10060672.

[16] B. G. Mekonnen, G. Bright, and A. Walker. CADCAM, Robotics and Factories of the Future. *Concurrent Engineering*, 21:307–307, 2013.

[17] J. L. Bartlett and X. Li. An overview of residual stresses in metal powder bed fusion. *Additive Manufacturing*, 27:131–149, 2019.

[18] H. Gong, K. Rafi, H. Gu, T. Starr, and B. Stucker. Analysis of defect generation in Ti-6Al-4V parts made using powder bed fusion additive manufacturing processes. *Additive Manufacturing*, 1:87–98, 2014.

[19] Q. Chen, G. Guillemot, C. A. Gandin, and M. Bellet. Three-dimensional finite element thermomechanical modeling of additive manufacturing by selective laser melting for ceramic materials. *Additive Manufacturing*, 16:124–137, 2017.

[20] J. L. Prado-Cerqueira, A. M. Camacho, J. L. Diéguez, Rodríguez-Prieto, A. M. Aragón, C. Lorenzo-Martín, and Yanguas-Gil. Analysis of Favorable Process Conditions for the Manufacturing of Thin-Wall Pieces of Mild Steel Obtained by Wire and Arc Additive. *Materials*, 11:1449, 2018.

[21] S. W. Williams, F. Martina, A. C. Addison, J. Ding, G. Pardal, and P. Colegrove. Wire + Arc Additive Manufacturing. *Materials Science and Technology*, 32:641–647, 2015.

[22] D. Ding, Z. Pan, D. Cuiuri, and H. Li. Wire-feed additive manufacturing of metal components: technologies, developments and future interests. *International Journal of Advanced Manufacturing Technology*, 81:465–481, 2015. ISSN 14333015.

[23] F. Martina, J. Mehnen, S. W. Williams, P. Colegrove, and F. Wang. Investigation of the benefits of plasma deposition for the additive layer manufacture of Ti-6Al-4V. *Journal of Materials Processing Technology*, 212:1377–1386, 2012.

[24] H. Geng, J. Li, J. Xiong, X. Lin, and F. Zhang. Optimization of wire feed for GTAW based additive manufacturing. *Journal of Materials Processing Technology*, 243:40–47, 2017.

[25] Fronius. CMT - The cold welding process for premium quality, 2019. URL `https://www.fronius.com/en/welding-technology/our-expertise/welding-processes/cmt`.

[26] P. M. Sequeira Almeida and S. Williams. Innovative Process Model of Ti-6Al-4V Additive Layer Manufacturing Using Cold Metal Transfer (Cmt). *SFF Symposium*, pages 25–36, 2010.

[27] E. Välimäki. *Modelling, Simulation and Validation of CMT Process: an Application for Additive Manufacturing*. PhD thesis, 2016.

[28] B. Mezrag, F. Deschaux-Beaume, and M. Benachour. Control of mass and heat transfer for steel/aluminium joining using Cold Metal Transfer process. *Science and Technology of Welding and Joining*, 20:189–198, 2014.

[29] M. Ashby, S. Hugh, and D. Cebon. *Materials: engineering, science, processing and desing*. 2014.

[30] R. Sun, L. Li, Y. Zhu, W. Guo, P. Peng, B. Cong, J. Sun, Z. Che, B. Li, C. Guo, and L. Liu. Microstructure, residual stress and tensile properties control of wire-arc additive manufactured 2319 aluminum alloy with laser shock peening. *Journal of Alloys and Compounds*, 747:255–265, 2018.

[31] P. A. Colegrove, F. Martina, M. J. Roy, B. A. Szost, S. Terzi, S. W. Williams, P. J. Withers, and D. Jarvis. High pressure interpass rolling of Wire + Arc additively manufactured titanium components. *Advanced Materials Research*, 996:694–700, 2014.

[32] A. Lopez, R. Bacelar, and T. G. Santos. Mapping of non-destructive techniques for inspection of wire and arc additive manufacturing. Number July 2018, 2017.

[33] A. Plessis, I. Yadroitsev, I. Yadroitsava, and S. G. L. Roux. X-Ray Microcomputed Tomography in Additive Manufacturing : A Review of the Current Technology and Applications. 5:227–247, 2018.

[34] G. Stephan, J. Els, G. Booysen, and D. C. Blaine. Case Studies in Nondestructive Testing and Evaluation Application of microCT to the non-destructive testing of an additive manufactured titanium component. *Case Studies in Nondestructive Testing and Evaluation*, 4:1–7, 2015.

[35] N. Montinaro, D. Cerniglia, and G. Pitarresi. A numerical and experimental study through laser thermography for defect detection on metal additive manufactured parts. *Frattura ed Integrita Strutturale*, 12:231–240, 2018.

[36] Olympus Inspection Solutions, https://www.olympus-ims.com/pt/, viewed on 2019-10-06.

[37] D. Pasadas, A. L. Ribeiro, and H. G. Ramos. Analysis of the magnetic field in the presence of linear sub surface cracks using ECT. *Acta Imeko*, 7:36, 2018.

[38] P. Vilac¸a, T. G. Santos, L. Rosado, and R. M. Miranda. Innovative concept and application of EC probe for inspection of friction stir welds. *International Journal of Microstructure and Materials Properties*, 9:314–326, 2014.

[39] T. Santos, P. Vilaça, J. D. Santos, and L. Quintino. A new NDT system for micro imperfections detection: Application to FSW and FSpW. *Weld. World*, (June 2014):6–11, 2009.

[40] Ultrasonic Testing FAQ, https://www.olympus-ims.com/en/knowledge/ultrasound/applications , viewed on 7 october.

[41] Introduction to Ultrasonic Testing, https://www.nde-ed.org/EducationResources, viewed on 7 october.

[42] L. W. Schmerr. Wave Motion Fundamentals. In *Fundamentals of Ultrasonic Nondestructive Evaluation*, pages 33–54. springer, 2016. ISBN 9783319304632. doi: 10.1007/978-3-319-30463-2{_}3.

[43] I. Ihara. Ultrasonic sensing: Fundamentals and its applications to nondestructive evaluation. *Lecture Notes in Electrical Engineering*, 21 LNEE:287–305, 2008.

[44] High Temperature Ultrasonic Testing, https://www.olympus-ims.com/en/applications/high-temperature-ultrasonic-testing/, viewed on 7 october.

[45] T. A. Rodrigues, V. Duarte, J. A. Avila, T. G. Santos, R. M. Miranda, and J. P. Oliveira. Wire and arc additive manufacturing of HSLA steel: Effect of thermal cycles on microstructure and mechanical properties. *Additive Manufacturing*, 27:440–450, 2019.

[46] Reflection and Transmission, https://www.nde-ed.org/EducationResources/CommunityCollege, viewed on 7 october.

[47] About NDT, https://www.bindt.org/What-is-NDT/, viewed on 8 october.

[48] R. Huang and L. W. Schmerr. Characterization of the system functions of ultrasonic linear phased array inspection systems. *Ultrasonics*, 49:219–225, 2009.

[49] Preparing Metal for Welding, http://www.halversoncts.com/95-preparing-metal-for-welding.html, viewed on 7 october.

[50] Y. Ali, P. Henckell, J. Hildebrand, J. Reimann, and J. P. Bergmann. Wire arc additive manufacturing of hot work tool steel with CMT process. *Journal of Materials Processing Tech.*, 269:109–116, 2019.

[51] A. Ermakova, A. Mehmanparast, and S. Ganguly. A review of present status and challenges of using additive manufacturing technology for offshore wind applications. *Procedia Structural Integrity*, 17: 29–36, 2019.

[52] X. Xu, J. Ding, S. Ganguly, C. Diao, and S. Williams. Preliminary Investigation of Building Strategies of Maraging Steel Bulk Material Using Wire + Arc Additive Manufacture. *Journal of Materials Engineering and Performance*, 28:594–600, 2018.

[53] J. Xiong, Y. Li, R. Li, and Z. Yin. Influences of process parameters on surface roughness of multi-layer single-pass thin-walled parts in GMAW-based additive manufacturing. *Journal of Materials Processing Technology*, 252:128–136, 2018.

[54] B. Helifa, A. Oulhadj, A. Benbelghit, I. K. Lefkaier, F. Boubenider, and D. Boutassouna. Detection and measurement of surface cracks in ferromagnetic materials using eddy current testing. *NDT and E International*, 39:384–390, 2006.

[55] B. Feng, A. L. Ribeiro, T. J. Rocha, and H. G. Ramos. Comparison of inspecting non-ferromagnetic and ferromagnetic metals using velocity induced eddy current probe. *Sensors (Switzerland)*, 18: 15–18, 2018.

[56] P. G. Benardos and G. C. Vosniakos. Predicting surface roughness in machining: A review. *International Journal of Machine Tools and Manufacture*, 43:833–844, 2003.

[57] Weld G3Si1, https://www.esab.co.uk/gb/en/products/filler-metals/mig-mag-wires-gmaw/mild-steel-wires/weld-g3si1.cfm, viewed on 21 october.